Validation of Simplified Urban-Canopy Aerodynamic Parametrizations Using a Numerical Simulation of an Actual Downtown Area

Copy edited by JNG: 6-8/2/18

Validation of simplified urban-canopy aerodynamic parametrizations using a numerical simulation of an actual downtown area

N. Ramirez • A. Afshari • L. Norford

Received: 7 December 2017 /
Accepted: 8 February 2018

~~Received: 10 December 2016~~

Abstract A steady-state Reynolds-averaged Navier-Stoke (RANS) computational fluid dynamics (CFD) investigation of boundary-layer flow over a major portion of downtown Abu Dhabi is conducted. The results are used to derive the shear stress and characterize the logarithmic region for eight sub-domains, where the sub-domains overlap and are overlaid in the streamwise direction. They are characterized by a high frontal area index initially, which decreases significantly beyond the fifth sub-domain. The plan area index is relatively stable throughout the domain. For each sub-domain, the estimated local roughness length and displacement height derived from CFD results are compared to prevalent empirical formulations. We further validate and tune a mixing-length model proposed by Coceal and Belcher (Quartely Journal of the Royal Meteorological Society, 2004, Vol.130, 1349-1372). Finally, the in-canopy wind-speed attenuation is analysed as a function of fetch. It is shown that, while there is some room for improvement in Macdonald's empirical formulations (Boundary-Layer Meteorology, 2000, Vol. 97, 25-45), Coceal and Belcher's mixing model in combination with the resolution method of Di Sabatino et al. (Boundary-Layer Meteorology, 2008, Vol.127, 131-151) can provide a robust estimation of the average wind speed in the logarithmic region. Within the roughness sublayer, a properly parametrized Cionco exponential model is shown to be quite accurate.

Keywords Morphological parameterization · Mixing-length model · Reynolds-averaged Navier-Stoke · Urban canopy model · Airflow

Accept

Afshin Afshari • Nicolas Ramirez, Masdar Institute of science and Technology, Abu Dhabi, United Arab Emirates (email: aafshari@masdar.ac.ae); Leslie Norford, Massachusetts Institute of Technology, Boston, USA

Sent to Iswarya: 8/2/18

cc. authors

29

30 **1 Introduction**

31 The consequences of anthropogenic activities in cities, such as the urban heat island and
32 air pollution, are mostly observed in the lower part of the urban boundary layer (UBL)
33 (Fernando 2010), and have been the basis for many studies that aim to understand air-flow
34 within cities (Barlow 2014). Thus, it is important to quantify the momentum transfer,
35 mixing and transport mechanisms that occur close to and above buildings within urban
36 areas.

37 From a purely aerodynamic point of view, the flow in and above the urban canopy layer
38 (UCL) is mostly affected by, (i) the existence of highly-turbulent overlapping shear layers
39 at the top of the urban canopy (Christen 2005), (ii) the result of complex interactions
40 between turbulence of different length scales (Coceal et al. 2007), and (iii) drag due to
41 roughness elements within the UCL (Giometto et al. 2016).

42 Numerous studies have been conducted in order to gain a better understanding of these
43 phenomena through numerical simulations (Sini et al. 1996; Baik and Kim 1999;
44 Assimakopoulos et al. 2003; Chan et al. 2003; Cheng et al. 2003; Bou-Zeid 2004; Coceal
45 et al. 2006; Xie and Castro 2006; Santiago et al. 2007; Xie et al. 2008; Letzel et al. 2008;
46 Xie 2011; Ramponi et al. 2015; Giometto et al. 2016); wind-tunnel experiments (Lettau
47 1969; Fang and Sill 1992; Meroney et al. 1996; Gerdes and Olivari 1999; Kastner-Klein
48 and Plate 1999; Brown et al. 2001; Cheng and Castro 2002a,b; Kastner-Klein and Rotach
49 2004; Barlow et al. 2004; Poggi et al. 2004; Pascheke et al. 2005) and field measurements
50 (Grimmond et al. 1998, 2004; Vachon et al. 2001; Toda and Sugita 2003; Emeis et al. 2004,
51 2007; Dobre et al. 2005; Li et al. 2010; Wood et al. 2010; Barlow et al. 2011; Emeis 2011;
52 Drew et al. 2013; Lane et al. 2013; Pelliccioni et al. 2016; Kent et al. 2017). Due to various
53 constraints, many of the numerical and wind-tunnel investigations simplify the urban

54 canopy by resorting to roughness elements that represent infinitely long rows of buildings
55 (Masson 2000, Martilli et al. 2007) or arrays of cubes/cuboids (Meinders and Hanjalić
56 1999; Hanna et al. 2002; Cheng and Castro 2002b; Stoesser et al. 2003; Kanda et al. 2004;
57 Coceal et al. 2006; Michioka et al. 2014; Zhu et al. 2016; Sadique et al. 2017).

58 The quasi-exclusive reliance of regular, cuboid-like, roughness elements in the current
59 literature is a significant limitation, since the arrangement, sizes and shapes of buildings in
60 a real urban setting are highly variable. Xie et al. (2008) performed large-eddy simulation
61 (LES) of flow over a more urban-like array of obstacles, based on wind-tunnel experiments
62 reported by Cheng and Castro (2002b), in which the height of a "repeating unit" varies.
63 They concluded that the flow within the canopy region generated by random height
64 buildings is significantly more complex than in the case of uniform height and that,
65 although spatially-averaged quantities and their spatial standard deviations are quite similar
66 in both random and uniform arrays, there are many features of the flow that cannot easily
67 be inferred based on what is known about the flow over isolated elements. Zhu et al. (2016)
68 attempted to characterize fully random urban-like topographies and derive aerodynamic
69 parameters through LES. However, the topographies considered were composed of
70 staggered distributions of square-based prisms. Similarly, Yang et al. (2016) and Sadique
71 et al. (2017) evaluated the aerodynamic properties of rough surfaces in LES by varying the
72 aspect ratio and arrangements of rectangular-prism-shaped elements. Due to steadily
73 increasing computational power, simulating real topographies is now possible, as seen in
74 three recent computational fluid dynamics (CFD) studies of Kanda et al. (2013) and
75 Giometto et al. (2016, 2017).

76 A city represents a sudden change in the surrounding surface roughness that affects
77 flow behaviour in and above it. Raupach et al. (1980) and Rotach (1995) have established
78 the existence of a roughness sublayer (RSL) below the inertial sublayer (ISL), where the

79 RSL is assumed to have a height of 2–5 times the average building height (Cheng and
80 Castro 2002b; Kastner-Klein and Rotach 2004) . Most studies point to the fact that, above
81 the RSL, a logarithmic profile for the flow velocity is observed. Nonetheless, Cheng and
82 Castro (2002b) show that the spatially-averaged mean velocity within the RSL can also be
83 described by the logarithmic law. The influence of the buildings or obstacles on this profile
84 is described through the aerodynamic roughness length z_0 and the zero-plane displacement
85 d (Santamouris and Asimakopoulos 2001). Experimental measurements allow z_0 to be
86 derived from the Reynolds-averaged velocity profile (Zhu et al. 2016). The practical
87 limitations of this approach are obvious, which is why several studies such as that by
88 Macdonald et al. (1998) propose to relate empirically these aerodynamic parameters to the
89 geometry of the roughness elements.
90 We compare CFD-derived roughness length and displacement height values for a real
91 urban site to those prescribed by empirical formulations found across the literature through
92 an extensive morphological analysis. We investigate the accuracy of the empirical models
93 when applied to a fully irregular geometry, and explore other approaches, such as the
94 mixing-length model, for the estimation of the average wind profile above the urban
95 canopy.
96 Coceal and Belcher (2004) developed a simple mixing-length model that is able to
97 represent the dynamical effects of urban areas without a roughness length, and give
98 estimates for the mean wind speed and turbulence in the RSL. Di Sabatino et al. (2008)
99 stated that the application of this model to real cities still needs to be validated, which we
100 attempt to do herein. To validate the model, it is necessary to calculate the drag coefficient.
101 Basing their calculations on the wind-tunnel measurements performed by Cheng and
102 Castro (2002b), Coceal and Belcher (2004) attempt to account for height in their
103 calculation of the canopy-element drag force. They introduce a drag coefficient varying

104 with height that is then integrated across the canopy depth. In their case, the fractional
105 volume occupied by air in the canopy is constant since they deal with regular arrays of
106 cubes. Extending their methodology in our CFD simulations, we calculate the total drag
107 force exerted by the roughness elements as a function of height, considering the real
108 volume of air at each height. Finally, we propose a modification of the model of Coceal
109 and Belcher (2004) and show that it achieves remarkably good fits to the CFD wind profile.
110 To summarize, we conduct a steady-state Reynolds-averaged Navier-Stoke (RANS)
111 CFD simulation over a substantial part of the city of Abu Dhabi wherein we introduce the
112 following novelties:
113 • Divide the domain into overlapping stripes, allowing us to analyse the evolution of the
114 urban boundary layer as the flow moves inland above stripes of varying morphology,
115 • Characterize the domain exhaustively through formally defined plan area and frontal
116 area indices that vary with height,
117 • Introduce an improved method to calculate the height-dependent drag coefficient in
118 real urban canopies using aforementioned height-dependent morphological indices,
119 • The height-dependence of the morphological indices and of the drag coefficient
120 propagate to multiple secondary parameters, resulting in original and enhanced
121 versions of the classical models used in the estimation of the zero-plane displacement,
122 the roughness length and the mixing-length,
123 • Further, we tune several experimentally determined parameters used in morphometric
124 methods as well as the mixing-length model, in order to adapt them to the case at hand
125 (City of Abu Dhabi),
126 • Analyse the in-canopy wind-speed reduction as a function of fetch for the City of Abu
127 Dhabi.
128

2 Computational Fluid Dynamics simulation

A three-dimensional model of the city was created using ArcGIS 10.2, a Geographic Information System (GIS) software, and data obtained from local authorities, and then imported to the CFD analysis software FLUENT® 16.2, by ANSYS Inc[1]. Best-practice modelling considerations are described below.

2.1 Weather stations

Data from weather stations were used to better understand predominant winds and average wind speeds and orient the computational domain accordingly, and later to validate our CFD analysis. Specifically, we relied on a weather station located in an unbuilt portion of Masdar City near the international airport (rural reference station) as well as ten stations in downtown Abu Dhabi (stations WS1 and WS2, part of Abu Dhabi Environmental Agency's infrastructure, and S1-S8, installed recently by the authors on light poles), shown in Fig. 1.

The weather station in Masdar City is assumed to provide rural weather conditions – and resemble typical airport data - due to its isolation and distance from Abu Dhabi downtown. Station WS1 is located along a main corridor close to the promenade while

[1] Ansys, Inc.: www.ansys.com

station WS2 is situated in the middle of a densely built district. Both weather stations have a sonic wind sensor and are located at a height of 10 m above ground level.

Hourly wind data from 2012-2015 were analysed in Fig. 1a, b, c, which show the wind roses for that year at stations WS1, WS2 and Masdar City, respectively. The urban stations, on the other hand, cover a period of six months in 2017 (April to September). Wind speed does not exhibit noteworthy seasonality in Abu Dhabi.

The predominant wind direction at Masdar City (rural) is north-north-west, with an average wind speed of 2.9 m s^{-1} at a height of 10 m above ground. Considering the atmospheric boundary layer (ABL) and the scale at hand, these conditions were assumed to be similar in the immediate proximity of the city of Abu Dhabi, and were therefore used to set the boundary conditions of the computational domain, which will be described in more detail in Sect. 2.4.

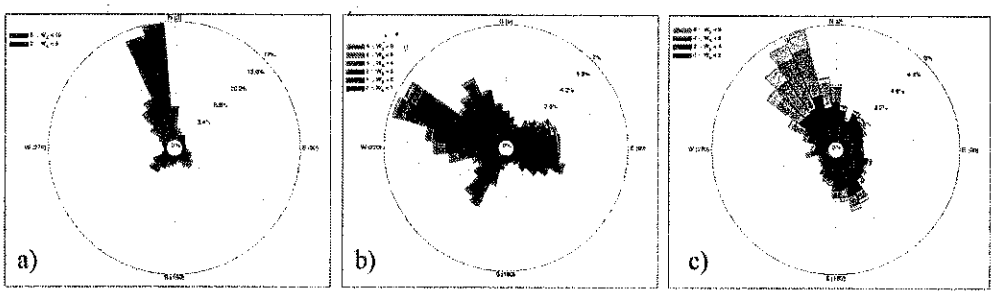

Fig 1 Wind roses for station WS1 (**a**), station WS2 (**b**) and Masdar City (**c**) for the period 2012-2015; and the geographical location of weather stations, wind sensors and Masdar City (**d**)

Experimental data show great disparity in wind direction and speed between rural and urban settings. The wind rose of the weather station that is closer to the water front (station WS1) resembles the rural weather station. The wind direction is similar due to the few obstacles (buildings) between station WS1 and the open sea. Nonetheless, the average wind speed is reduced due to the urban canopy – from 2.9 m s^{-1} to 2.0 m s^{-1}. This effect is accentuated when analysing the results from station WS2. Average wind speeds are reduced by almost 40% – from 2.9 m s^{-1} to 1.8 m s^{-1} – and the predominant wind direction is less obvious due to the distribution of buildings surrounding the weather station.

The eight sonic anemometers (S1-S8) located in the heart of the computational domain, at a height of six meters above ground level, provided further wind speed and direction data. Eight months of data were available and analysed, as seen later on in Table 1.

2.2 Domain of study

The horizontal scale should include the whole city and its surroundings. Nonetheless, we choose to limit the domain to a portion of downtown comprising about 1,400 buildings in order to render the CFD problem more manageable computationally. Although the effect of vegetation on momentum is found to be notorious (Giometto et al. 2017), it is neglected in our domain due to the scarcity of greenery. The domain comprises 11 districts.

Close to ~~fourteen hundred~~ 1400 buildings located along the promenade were simulated, with a total built ground area of approximately 3.6 km^2. The domain is long enough to capture how the low-level flow penetrates the city and wide enough to consider the influence of surrounding buildings. The COST 732 Best Practice Guideline for CFD simulation of flow

(h is building height)

in the urban environment (Franke et al. 2011) recommends the vertical dimension of the computational domain to be six times the height of the tallest building ($6h_{max}$). In our simulation, this height corresponds to 900 m. Similarly, it suggests that for urban areas with multiple buildings, the lateral boundaries of the computational domain should be placed at $5h_{max}$ from the nearest obstacle. However, since the influence of the lateral boundaries on the flow and dispersion is highly case dependent, it is recommended to test different distances. We find that the suggested value of $5h_{max}$ is not enough, and that only after $7h_{max}$ is no local acceleration present. The region behind an isolated building should be at least $15h$ to allow for flow re-development behind the wake (Cowan et al. 1997; Bartzis et al. 2004). Although it is not the case, we assume the worst-case scenario, where the tallest building would be in the last row of the modelled buildings. Finally, even though there are discrepancies between authors, Bartzis et al. (2004) recommend $8h_{max}$ as the longitudinal extension of the domain in the region in front of the built area. Figure 2 summarizes these parameters. The total size of the computational domain is 28.9 km^2 (6.25 km × 4.62 km).

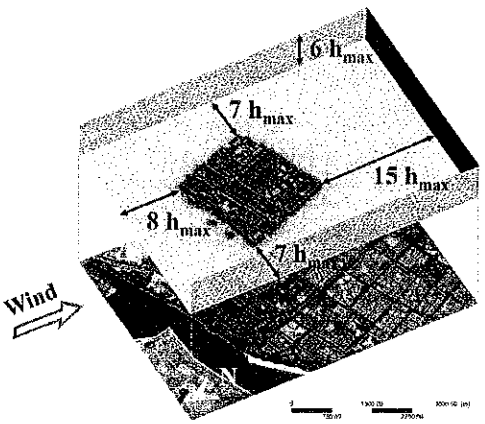

Fig 2 Computational domain

202

203 2.3 Grid

204 The computational grid resolution was determined taking into consideration best practice
205 guidelines discussed by Franke et al. (2004) and Tominaga et al. (2008). The former states
206 that the grid should be fine enough to capture such important physical phenomena as shear
207 layers and vertical structures with sufficient resolution, while allowing a large enough
208 computational domain so as not to have a strong artificial acceleration. The latter authors
209 above advise that the grid should capture the characteristics of separating flows on roofs
210 and walls. Following the arrangement of grid cells near a solid surface in an unstructured
211 grid as advised by Tominaga et al. (2008), where the surface mesh is wrapped by prismatic
212 elements initially and then by tetrahedral elements, we made use of 10 boundary-layer
213 elements on the surfaces of all buildings in the centre of the domain and the ground.
214 Logarithmic-law wall functions can only be applied if the first element of the mesh is a
215 distance from the wall that falls inside the logarithmic region. In FLUENT®, this region is
216 assumed to be between $30 < y^+ < 300$, where y^+ is defined as

$$y^+ = \frac{u_* y}{\nu}, \quad (1)$$

217 and where u_* is the friction velocity at the wall, y is the distance to the wall and ν is the
218 local kinematic viscosity of the fluid. The average y^+ values for buildings and the ground
219 are 140 and 180, respectively, where the maximum values are under 550 in both cases. The
220 finest resolution of the first-layer thickness, y, is 0.03 m. The rest of the mesh was filled
221 with four-node tetrahedral cells, following a proximity sizing control where the elements

become finer the closer they are to the building's surfaces and edges, as seen in Fig. 3a, b.

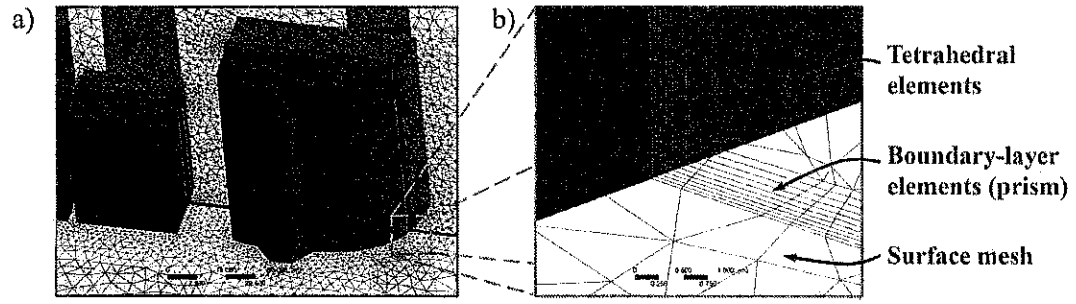

Fig 3 Proximity sizing control on surface mesh (**a**), and arrangement of grid cells near a solid surface in an unstructured grid (**b**)

According to the ANSYS mesh quality spectrum, both maximum skewness and minimum orthogonal quality are acceptable in the metrics' spectra, with average values of 0.25 (excellent) and 0.85 (very good) for skewness and orthogonal quality, respectively.

An iterative process was used to improve the mesh in strategic areas through adaptive refinement once the solution had converged. Mean velocity, turbulence kinetic energy (TKE) and TKE dissipation rate gradients dictated the refinement areas in order to resolve the wake regions accurately, where the gradient refinement threshold chosen was 10. The mesh, initially made of 48×10^6 cells, reached 52×10^6 cells after four mesh refinement iterations.

2.4 Boundary conditions

Inlet boundary conditions account for the upstream aerodynamic roughness length and describe vertical profiles for mean velocity and turbulence properties (Blocken 2015). Ideally, data from an offshore weather station would be directly used for the inlet boundary conditions. Unfortunately, these data were not available, which is why the incoming wind

242 profile was assumed to be similar to (but not exactly the same as) that of a rural weather
243 station in Masdar City.
244 The COST 732 *Best Practice Guideline for the CFD Simulation of Flows in the Urban*
245 *Environment* (Franke et al. 2011) recommends the relations suggested by Richards and
246 Hoxey (1993), in which, assuming constant stress with height, the vertical profiles for the
247 horizontal wind speed $U(z)$, TKE $k(z)$ and the TKE dissipation rate $\varepsilon(z)$ in the ABL are

$$U(z) = \frac{u_*}{\kappa} \ln\left(\frac{z}{z_0}\right), \tag{2}$$

$$k(z) = \frac{{u_*}^2}{\sqrt{C_\mu}}, \tag{3}$$

$$\varepsilon(z) = \frac{{u_*}^3}{\kappa(z + z_0)}, \tag{4}$$

248 where κ is the von Karman constant, taken to be 0.40, C_μ is a constant, generally taken
249 equal to 0.09, u_* is the friction velocity and z_0 is the roughness length.
250 Experimental data were used to quantify the roughness length and friction velocity
251 accurately. Wind sensors at different heights (10, 30, 40, 49, 50 m) were used to
252 approximate the wind profile at Masdar City during the period 2012–2015. The roughness
253 length and friction velocity at Masdar City were calculated through an iterative process
254 using the least squares method, giving $z_0 = 0.08$ m, and $u_* = 0.26$ m s^{-1}.
255 The friction velocity is intimately related to the level of turbulence in the lowest level
256 of the atmosphere (Cushman-Roisin 2014). Around 1000 m above the surface of the Earth,
257 Erell et al. (2012) conclude that the geostrophic wind velocity is the same over different
258 terrains (A and B), and derive a relationship between the respective z_0 and u_* values,

$$\frac{u_{*B}}{u_{*A}} = \left(\frac{z_{0B}}{z_{0A}}\right)^{0.09}, \tag{5}$$

from neutral wind profiles

259 which is used to extrapolate the friction velocity from Masdar City to the inlet of the
260 computational domain. The existence of Lulu Island, directly in front of the city's
261 promenade, was not modelled explicitly but instead, a z_0 ~~value of~~ 0.1 m was assumed,
262 following the roughness classification of Wieringa (1992). The friction velocity for ~~that~~ the
263 final inlet profile is 0.28 m s^{-1}.

264 Following Franke et al. (2011) regarding large computational domains, the inviscid
265 wall condition was imposed to the lateral surfaces to make the computation more stable;
266 i.e. the normal velocity component and normal gradients of tangential velocity components
267 was set to zero. The boundary condition corresponding to the ground surface and building
268 surfaces is non-slip, while the sky can be considered a symmetry plane or pressure outlet
269 due to the assumed parallel and horizontal behaviour of the ~~wind~~ flow at those heights.

270 At the outlet of the domain, zero static gauge pressure was imposed.

271

272 2.5 CFD solution algorithm

273 COST 732 (Franke et al. 2011) concludes that the standard k-ε model should not be
274 used in simulations for wind engineering problems, whereas the realizable k-ε turbulence
275 model offers good performance for airflow around buildings (Franke 2006). Regarding
276 convergence, scaled residuals should be decreased by four orders of magnitude (Franke et
277 al. 2004).

278 The three-dimensional steady RANS equations for incompressible and isothermal flow
279 were solved in combination with the realizable k-ε turbulence model in a parallel
280 computing environment with 50 cores. The semi-implicit method for pressure linked
281 equations (SIMPLE) algorithm was used. Pressure interpolation was second order and
282 second-order discretization schemes were used for both the convection terms and the
283 viscous terms of the governing equations. Convergence was achieved when all scaled

residuals and some control monitors (maximum velocity and TKE, average velocity and TKE and drag coefficient in district E3, located in the centre of the domain) reached quasi-constant values. The scaled residuals of continuity, k and ε decreased by more than 6×10^{-4}, and of the three velocity components by more than 1×10^{-5}.

2.6 Validation

The two weather stations WS1 and WS2 and eight wind sensors (S1-S8), described in Sect. 2.1 registered the wind direction and speed over different time periods – years 2012 to 2015 for the weather stations and eight months in 2017 for the wind sensors. The weather stations are operated by the Environmental Agency of Abu Dhabi. The measurements, averaged over the full measurement period, were used to validate the CFD simulation as shown in Table 1. A root-mean-squared error (*RMSE*) of 0.067 was obtained for the wind speed, which is close to 5% of the mean value of all the stations. For wind direction, the difference between the predominant wind direction, given by the wind rose of each wind sensor, and the CFD results at the same locations was computed, such that the average error was of 11°. Note that the measurement height is different for the weather stations and the wind sensors.

	Location	Experimental wind speed ($m\ s^{-1}$)	CFD wind speed ($m\ s^{-1}$)	Experimental wind direction (°)	CFD wind direction (°)
Masdar City		2.8	-	-	-
WS1	24.488928°N 54.363717°E	2.0	2.0	-	-
WS2	24.481558°N 54.369331°E	1.8	1.6	-	-
S1	24.489352°N 54.361546°E	1.2	1.1	171	142

S2	24.491396°N 54.365592°E	1.5	1.5	22	222
S3	24.483709°N 54.359425°E	1.7	1.8	81	77
S4	24.494263°N 54.372029°E	0.9	0.9	73	80
S5	24.483377°N 54.374603°E	1.3	1.3	51	55
S6	24.490045°N 54.365214°E	1.3	1.2	120	141
S7	24.489157°N 54.366743°E	1.4	1.4	116	134
S8	24.490655°N 54.365984°E	1.4	1.5	112	116

Table 1 CFD validation and flow comparison

2.7 Spatial averaging

All the results shown herein have been calculated using spatial averaging in such a way that mean values across planes are computed using the area-weighted average, which considers the cell sizes in that plane. Furthermore, data was only obtained across the air surrounding the buildings.

Numerically, the averaged values are derived as follows

$$\langle \bar{\psi} \rangle_k = \sum_i \sum_j A \, \bar{\psi}_{i,j,k} / \sum A \,, \tag{6}$$

where ψ is a scalar field defined in the air but not at points occupied by canopy elements, A is the cell area, $\sum A$ is the total area of the air region.

Post-simulation, in order to analyse the results in a meaningful way, the domain was divided into eight sections, or stripes, longitudinally perpendicular to the prevailing wind direction (Fig. 4). Note that there are still buildings in front of stripe "a" and beyond stripe "h", as will be discussed further in Sect. 3.6.

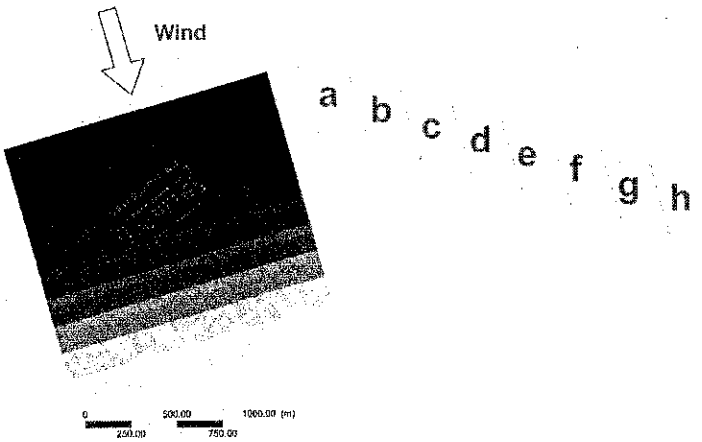

Fig 4 Stripe codes

Each stripe has dimensions of 400 m × 1500 m, enclosing an area of 0.6 km^2, ~~Each~~ stripe ~~is~~ offset, in the streamwise direction, by 150 m with respect to the previous stripe. Hence, the stripes are *overlapping*. This was done to ensure a certain regularity and continuity when analysing the morphological determinants of consecutive stripes, while still capturing the change brought by the inland progression. We refer to the stripes as stripe "a", stripe "b" … stripe "h". The total domain comprising the eight overlapping stripes ~~will be called~~ 'all-stripes'.

3 Case study: results and discussion

The case study consists of applying the simulation and data analysis methodologies to the specified large area within the city of Abu Dhabi. The semi-logarithmic plot displayed in Fig. 5 for the all-stripes domain shows that the streamwise velocity component exhibits logarithmic-law behaviour, characteristic of the urban inertial sublayer, roughly in the

331 region $z \in [50\text{ m}, 150\text{ m}]$. At higher elevations and above a transition region, the rural
332 atmospheric logarithmic law can be seen to still prevail.

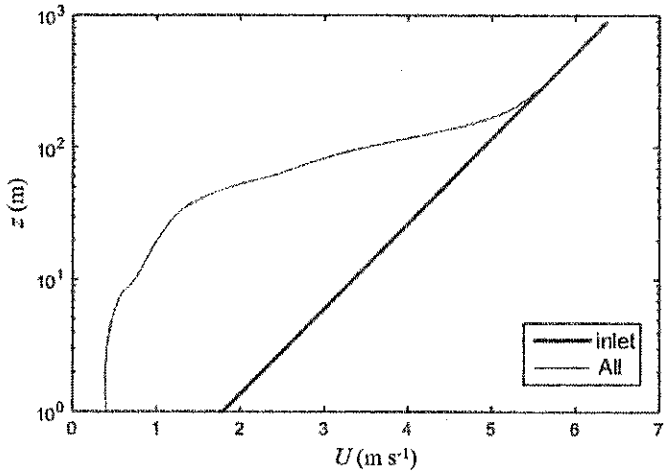

333

334 **Fig 5** Semi-logarithmic plot of the streamwise velocity component as a function of height for the all-stripes
335 domain

336

337 3.1 Morphological analysis

338 The most basic geometric parameters that describe the morphology of groups of buildings
339 are the plan area index (λ_P) and frontal area index (λ_F), defined as the ratio of building
340 plan area to total plot area and building frontal area to the plot area, respectively. These
341 simple parameters have been used extensively in empirical relations derived to predict z_0
342 and d (Lettau 1969; Counehan 1971; Raupach 1992, 1994; Bottema and Mestayer 1998;
343 Macdonald et al. 1998; Kastner-Klein and Rotach 2004) although more recently developed
344 models also account for variability in the height of buildings (Millward-Hopkins et al.
345 2011; Kanda et al. 2013; Zhu et al. 2016). Kanda et al. (2013) demonstrate, in a LES of the
346 city of Tokyo, that a peak in momentum flux exists between the standard deviation of

roughness-element heights plus the average height, $\sigma_h + h$, and the maximum building height, h_{max}, and thus these heights are likely to be important. Furthermore, Zhu et al. (2016) conduct LES of synthetic urban-like topographies built on regular square structures, and argue that statistical moments of the topography, in particular the standard deviation, $\langle \sigma_h \rangle$, and skewness, $\langle s_k \rangle$, are closely related to z_0. We note that Zhu et al. (2016) account for ground surface in their calculations. For real urban topologies of varying plot sizes, the last-mentioned parameters are formally defined as

$$\langle \sigma_h \rangle = \left[\frac{1}{n-1} \sum_i^n \left(n h_i \frac{A_{Pi}}{A_T} - \langle h \rangle \right)^2 \right]^{1/2}, \tag{7}$$

$$\langle s_k \rangle = \frac{\frac{1}{n-1} \sum_i^n \left(n h_i \frac{A_{Pi}}{A_T} - \langle h \rangle \right)^3}{\left[\frac{1}{n-1} \sum_i^n \left(n h_i \frac{A_{Pi}}{A_T} - \langle h \rangle \right)^2 \right]^{3/2}}, \tag{8}$$

where n is the number of units; i.e. $n-1$ buildings plus 1 ground surface, A_T the total lot size, h_i and A_{Pi} the height and plan area of building i, respectively, and $\langle h \rangle$ is the plan-area average building height, considering the ground

$$\langle h \rangle = \frac{1}{n} \sum_i^n n h_i \frac{A_{Pi}}{A_T}. \tag{9}$$

This mean height, $\langle h \rangle$, can also be thought of as the height of the rectangular prism that has the same volume as all the buildings and a base of A_T.

The main morphological characteristics of the stripes, defined above, are shown in Table 2, where the fetch is the distance from the shore to the stripe measured at the centroid of each stripe. The volumetric average height, $h_V = \frac{\sum_i^n V_i h_i}{\sum_i^n V_i}$, is also calculated, with h_P and h_F defined further below.

Stripe	Fetch (m)	h_{max} (m)	λ_P (-)	λ_F (-)	h_P (m)	h_F (m)	$\bar{h}$ (m)	σ_h (m)	s_k (-)	$\langle h \rangle$ (m)	$\langle \sigma_h \rangle$ (m)	$\langle s_k \rangle$ (×1000)	h_V (m)
a	200	115.2	0.26	0.63	44.1	39.3	33.8	25.9	0.49	11.3	14.7	1.73	57.7
b	350	108.8	0.28	0.65	42.1	37.5	32.1	22.8	0.31	11.7	17.5	1.57	52.9
c	500	96.0	0.29	0.66	40.5	36.0	31.5	21.2	0.34	11.7	18.3	1.61	51.2
d	650	96.0	0.29	0.59	34.7	31.7	28.2	19.9	0.63	10.0	15.9	3.10	47.4
e	800	96.0	0.29	0.51	29.0	26.8	23.5	19.3	1.03	8.52	12.6	4.15	45.4
f	950	73.6	0.30	0.39	21.7	20.7	17.9	17.8	1.55	6.59	11.0	4.65	41.5
g	1100	73.6	0.32	0.32	18.5	17.9	15.3	16.4	1.98	5.85	10.9	4.81	37.8
h	1250	70.4	0.32	0.31	16.5	16.4	14.7	14.1	2.17	5.35	10.3	7.27	32.3
All	-	115.2	0.27	0.47	30.4	28.0	24.2	21.5	1.07	29.7	25.3	-0.09	48.6

Table 2 Geometric parameters of the stripes

A priori, we are sceptical about the performance of morphological methods based on the assumption that the distribution of building heights is Gaussian, due to the fact that this is not the case for any of the stripes under consideration herein. As with Giometto et al. (2016), the density function of roof heights is multi-modal (four in our case), as seen in Fig. 6d for the all-stripes domain. Millward-Hopkins et al. (2013) suggest that σ_h may be used to estimate aerodynamic parameters of vertically heterogenous surfaces when a high degree of precision is not required.

Thus, we are inclined to find other ways to characterize the topology of real cities. The height distribution of buildings can be well represented by the vertical profile of the plan or frontal area indices, $\lambda_P(z)$ and $\lambda_F(z)$, respectively (Millward-Hopkins et al. 2013). Several studies have attempted to incorporate these height-dependent parameters in their analyses (Di Sabatino et al. 2008; Millward-Hopkins et al. 2013; Giometto et al. 2016), but

have failed to define them formally for an arbitrary geometry. The topology of the stripes can be characterized using the vertical variation of the sectional values of the plan area index $\lambda_P(z)$ and the frontal area index $\lambda_F(z)$ as seen in Fig. 6a, b, where $\lambda_P(z)$ and $\lambda_F(z)$ are defined as

$$\lambda_P(z) = \frac{A_P(z)}{A_T}, \tag{10}$$

$$\lambda_F(z) = \frac{h_F\, P_F(z)}{A_T}, \tag{11}$$

where

- $A_P(z) = \sum A_{Pi}\,(z)$ is the cross-sectional plan area of all buildings at height z;
- $A_{Pi}(z)$ is the cross-sectional plan area of building i at height z;
- $P_F(z) = \sum P_{Fi}(z)$ is the sum of projections of the perimeters of all buildings, at height z, onto the plane perpendicular to the flow direction;
- $P_{Fi}(z)$ is the projected perimeter of building i at height z, onto the plane perpendicular to the flow direction;
- $h_F = \frac{\sum h_i\, dA_{Fi}(0)}{\sum dA_{Fi}(0)} = \frac{\sum h_i\, P_{Fi}(0)dz}{\sum P_{Fi}(0)dz} = \frac{\sum h_i\, P_{Fi}(0)}{\sum P_{Fi}(0)}$ is the frontal-area-weighted average height of buildings;
- $h_P = \frac{\sum h_i\, A_{Pi}(0)}{\sum A_{Pi}(0)}$ is the plan-area-weighted average height of buildings; and
- h_i is the height of building i.

Strictly speaking, h_F is the differential frontal-area-weighted average height at ground level, such that at this height ($z = 0$) Eqs. 10 and 11 simplify to the standard definitions of plan and frontal area indexes, respectively, for any surface, unlike the scaling parameter used by Di Sabatino et al. (2008). Furthermore, $\lambda_F(z)$ can be re-arranged in terms of the

ratio between the frontal perimeters at ground level and z, and the common definition of frontal area as $\lambda_F(z) = \frac{P_F(z)}{P_F(0)} \frac{A_F}{A_T} = \frac{P_F(z)dz}{P_F(0)dz} \frac{A_F}{A_T} = \frac{dA_F(z)}{dA_F(0)} \frac{A_F}{A_T}$. In other words, the frontal area index tells us how much surface is exposed to the flow at height z, with respect to that at ground level.

The base values (i.e., at $z = 0$) of λ_P for different stripes vary little—approximately from 0.26 to 0.32—while the base values of λ_F show higher variability—varying approximately from 0.31 to 0.63. Figure 6c presents a *x-y* scatter plot of the base values of both indexes, where the 'x' symbol represents the individual stripes and the '*' symbol represents the all-stripes domain. They are normalized by the plan-area-weighted average height of buildings for the all-stripes domain, $h_0 = 30.4$ m. The initial stripes are characterized by high plan area index and high frontal area index, characteristic of high-rise buildings, where the last stripes are slightly denser and have lower frontal area index, indicating that the buildings are more cube-like. The ratio of h/h_0 for stripes "a" through "h" gradually decreases from about 1.5 to about 0.5 denoting that, as we advance inland, low- and mid-rise buildings become more and more prevalent. The frontal-area-weighted average h_F is always very close to, albeit slightly lower, than h (between 0.9 and 1). The ratio of the height of the tallest building to the average building height gradually increases from about 2-2.5 in stripes "a" through "d" to about 4 in stripe "g" (all-stripes ≈ 3.5). This denotes a regularly increasing level of relative heterogeneity as we progress inland.

a) **b)**

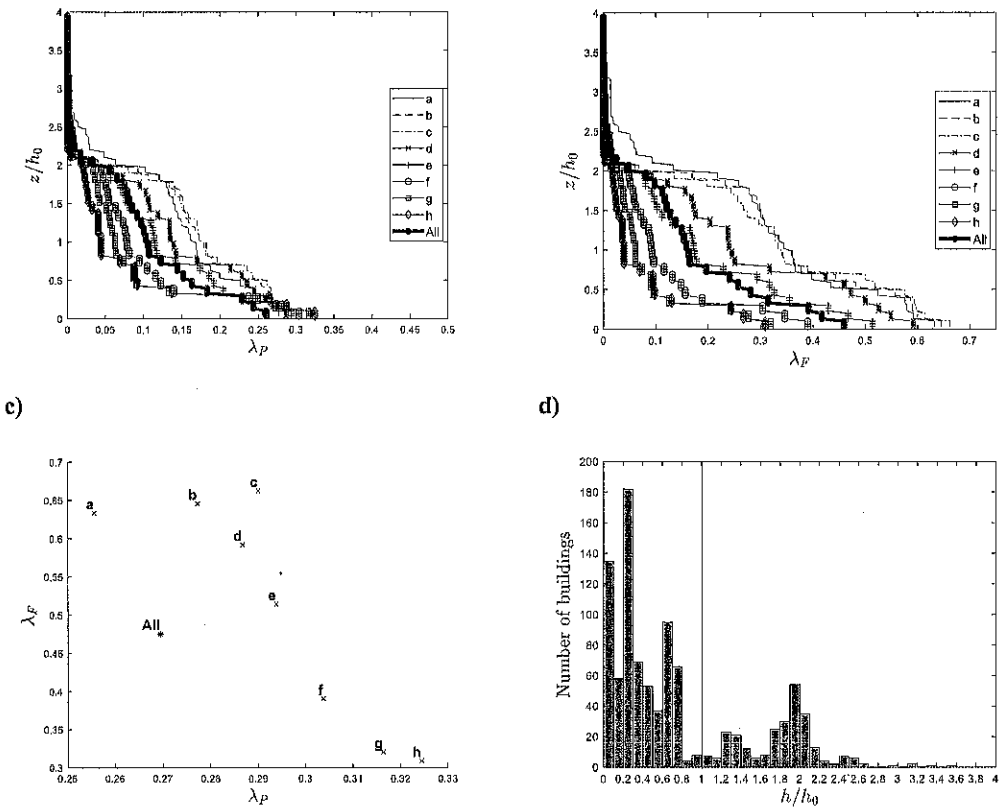

Fig 6 Normalized sectional $\lambda_F(z)$ (**a**), sectional $\lambda_P(z)$ (**b**), scatter plot of $\lambda_F(z)$ as a function of $\lambda_P(z)$ (**c**), and frequency distribution of building heights (**d**)

3.2 Shear stress

Let u_i be the velocity component in direction i where the subscript i represents one of the following directions or components: streamwise ($i = 1$, x axis), spanwise ($i = 2$, y axis) and vertical ($i = 3$, z axis). Further assume that angled brackets represent spatial averaging while the overbar represents time averaging. u_i comprises the following components

$$u_i = U_i + \tilde{u}_i + u_i' , \tag{12}$$

where U_i is the time- and space-averaged velocity component in direction i ($U_i = < \bar{u}_i >$), $\tilde{u}_i$ is the dispersive fluctuation or spatial variation of the time averaged value ($\tilde{u}_i = \bar{u}_i - U_i$) and u_i' is the turbulent fluctuation ($u_i' = u_i - U_i - \tilde{u}_i$).

As shown by Raupach and Shaw (1982) and Finnigan (2000), the mean velocity component in direction i, U_i, is obtained by solving the time- and space-averaged momentum equations. The averaging procedure produces four relevant terms in the momentum equation: a spatially-averaged Reynolds (or turbulent) stress $-< \overline{u_i' u_j'} >$, which represents spatially-averaged momentum transport due to turbulent velocity fluctuations; a dispersive stress $-< \tilde{u}_i \tilde{u}_j >$, due to momentum transport by the spatial deviations from the spatially-averaged velocity component; and finally the form and viscous drag forces imposed by the canopy f_D and f_v, respectively.

The total shear stress is the sum of the Reynolds stress and the dispersive stress,

$$\tau_{ij}/\rho = -< \overline{u_i' u_j'} > -< \tilde{u}_i \tilde{u}_j > . \tag{13}$$

The high-resolution CFD simulation of the time-averaged (mean) flow in the urban canopy is used to calculate the dispersive stresses directly, and the turbulent stresses through the Boussinesq approximation employed in the realizable k-ε turbulence model.

It is important to note that, unlike previous studies (e.g., Cheng and Castro 2002a,b; Coceal and Belcher 2004; Coceal et al. 2006; Xie et al. 2008), we perform a thorough spatial average across each cell, rather than computing values at strategically chosen points. For this reason, our results compare better to those studies that perform a similar spatial average, as in Martilli and Santiago (2007) and Lien and Yee (2004). We find that dispersive stresses show similar tendencies to those reported by Martilli and Santiago (2007) for a regular array of cubes: they decrease with fetch. However, it is clear that dispersive stresses

449 are important above the average building height for our highly heterogenous morphology.
450 In fact, all of stripes seem to reach the first maximum peak at about 2-3h, as seen in Fig.
451 7a. The height at which dispersive stresses become negligible also increases with fetch, as
452 the internal boundary layer (IBL) created by each stripe is superimposed and combined
453 with that of downstream stripes.

454 The same phenomenon can be seen in Fig. 8b, where the shear stress reaches several
455 local maxima. There is some evidence of a constant shear stress region appearing as the
456 IBL begins to develop above the roughness elements, reaching a maximum τ. Above this
457 region, the shear stress begins to decrease until it merges with the upstream IBL(s); we call
458 the latter the combined boundary layer. It extends until the top of the urban boundary layer
459 or the bottom of the rural boundary layer. In other words, the lowest region of quasi-
460 constant friction velocity defines the IBL while, above it, one often encounters a second
461 region of constant friction velocity, referred to as the combined boundary layer, since it
462 combines the effect of preceding stripes. The separation between the IBL and the combined
463 boundary layer can be observed from stripe "e" onwards, as seen in Fig. 8b. Within the
464 urban canopy layer, the shear stress carried by the fluid tends to zero with decreasing height
465 as the buildings take up part of the stress through the drag forces exerted on them.
466

a) b)

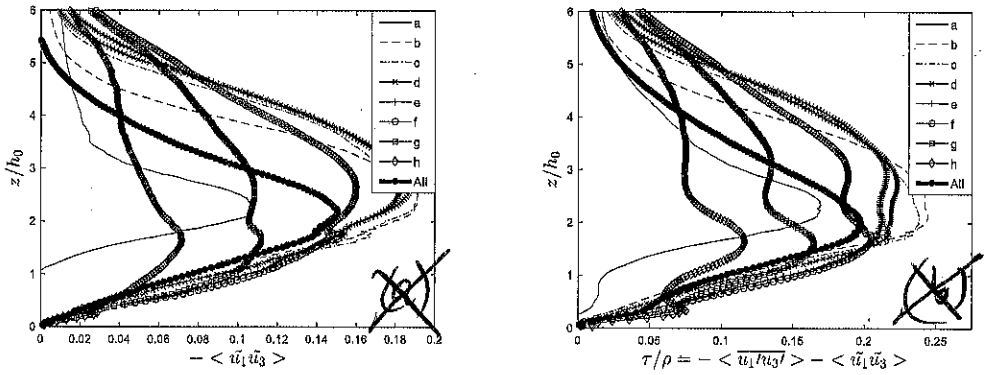

Fig 7 Dispersive stress (**a**), shear stress (**b**)

3.3 Drag coefficient

There is a dynamic balance between the vertical total stress gradient and the drag force within the canopy, and following Macdonald (2000), we apply an energy balance to a thin layer of height dz. The total drag force – the sum of viscous and form drag – acting on all canopy roughness elements in the streamwise direction at height z, $F_1(z)$, is equivalent to the momentum loss,

$$A_T\big(1-\lambda_P(z)\big)d\big(-\rho(<\overline{u_1'u_3'}>+<\tilde{u}_1\tilde{u}_3>)\big) = F_1(z). \tag{14}$$

Therefore,

$$\frac{d\big(<\overline{u_1'u_3'}>+<\tilde{u}_1\tilde{u}_3>\big)}{dz} = \frac{F_1(z)}{-\rho A_T\big(1-\lambda_P(z)\big)dz} = f_1(z) \tag{15}$$

where ρ is the density of air, $F_1(z)$ is the sectional streamwise component of the drag force, and $f_1(z)$ is the sectional streamwise component of the drag force per unit of air volume.

480 Figure 8 presents the sectional streamwise component of the drag force per unit of air
481 volume, $f_1(z)$, derived from CFD and morphological data as per Eq. 15. Stripe "a" converts
482 most of the flow momentum into drag as it is the first stripe the flow encounters and has
483 the highest frontal area index. Thereafter, each stripe exerts decreasing drag on the
484 incoming flow as we move inland.

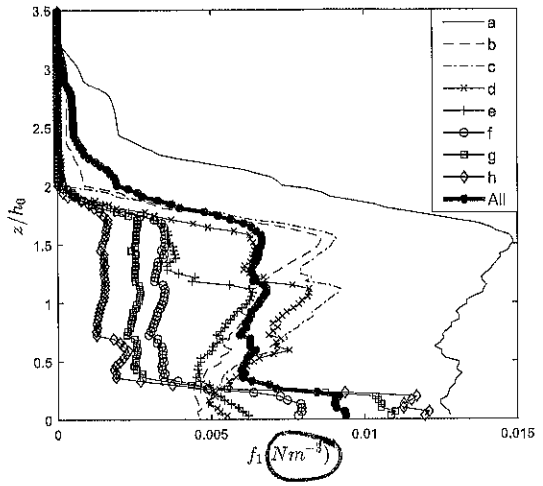

485

486 **Fig 8** Streamwise drag force per unit of air volume, $f_1(z)$

487

488 The streamwise drag force component per unit of (canopy air) volume can also be
489 defined by the drag equation as

$$f_1(z) = \frac{\rho}{2} c_d(z)|U(z)|U_1(z)\frac{P_F(z)dz}{A_T\big(1-\lambda_P(z)\big)dz},$$

$$= \frac{\rho}{2h_F} c_d(z)|U(z)|U_1(z)\frac{A_T\lambda_F(z)dz}{A_T\big(1-\lambda_P(z)\big)dz}, \qquad (16)$$

490 or,

$$f_1(z) = \frac{\rho}{2h_F} c_d(z)|U(z)|U_1(z)\frac{\lambda_F(z)}{1-\lambda_P(z)} = \rho\frac{|U(z)|U_1(z)}{L_c(z)}, \quad (17)$$

where, loosely following Coceal and Belcher (2004), the canopy drag length $L_c(z)$ is defined as

$$L_c(z) = \frac{2h_F}{c_d(z)}\frac{1-\lambda_P(z)}{\lambda_F(z)}. \quad (18)$$

From Eq. 17, we can derive the sectional drag coefficient, $c_d(z)$

$$c_d(z) = 2h_F\frac{1-\lambda_P(z)}{\lambda_F(z)}\frac{f_1(z)}{\rho|U(z)|U_1(z)}. \quad (19)$$

Similarly, the total drag force on canopy roughness elements can be expressed as a function of the depth-integrated drag coefficient, C_{dh}

$$\int_{z=0}^{h} F_1(z)dz = \frac{\rho C_{dh}A_F}{2h_F}\int_{z=0}^{h}|U(z)|U_1(z)dz \rightarrow C_{dh} = \frac{2h_F\int_{z=0}^{h}F_1(z)dz}{\rho A_F\int_{z=0}^{h}|U(z)|U_1(z)dz}, \quad (20)$$

where A_F is the total frontal area of all buildings, or $A_F = P_F(0)h_F$. Here, C_{dh} accounts for the average drag force acting on the buildings, assuming that the drag coefficient is constant throughout the canopy.

The results, for each stripe and for the whole domain, are presented in Fig. 9a, b. To be consistent with Coceal and Belcher (2004) and other studies focusing on arrays of cubes or cuboids, c_d is averaged within the urban canopy only (i.e. from the ground to h) rather than from the ground to h_{max} (height of the highest building). $\overline{c_d}$ varies between ≈ 0.29 and ≈ 4.5 (all-stripes domain: 0.88) while C_{dh} varies between ≈ 0.38 and ≈ 3.6 (all-stripes domain: 1.5).

506

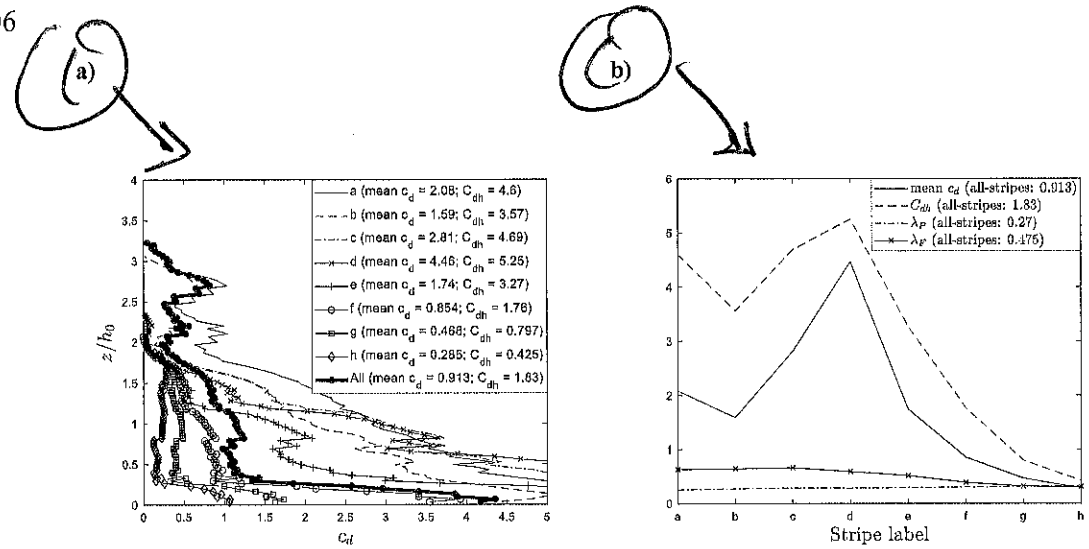

507 **Fig 9** Sectional drag coefficient $c_d(z)$ **(a)**, and average drag coefficient C_{dh} **(b)**

508

509 Our values of C_{dh} are larger than those reported by Coceal and Belcher (2004) for
510 stripes with high rise buildings ($C_{dh} = 4.6$ for stripe a versus $C_{dh} = 2.8$ for tall cuboids
511 per Coceal and Belcher (2004)), and smaller for stripes with more cubic arrangements
512 ($C_{dh} = 0.8$ for stripe "g" versus $C_{dh} = 1.2$ for cubes per Coceal and Belcher (2004)).
513 Furthermore, the $\overline{c_d}$ values reported by Coceal and Belcher (2004) are only calculated
514 above $z/h > 0.3$. Below these heights the sectional drag coefficient is substantially larger
515 in all the stripes, as seen in Fig. 9a. Lien and Yee (2005) also report this behaviour. There
516 is a large increase in both $\overline{c_d}$ and C_{dh} for stripe "d" due to the fact that the wind speed is
517 very close to zero near the ground, making the sectional drag coefficient very large (Fig.
518 9a) in the bottom part of the UCL. This phenomenon is also present in other stripes (a, c,
519 d, e), although it is not as evident.

520 The variation of the drag coefficient C_{dh} with increasing fetch is shown in Fig. 9b. Our
521 approximation of the average canopy drag length, L_c, assumed to be constant across the
522 urban canopy, is

$$\frac{L_c}{h} = \frac{2}{\overline{c_d}} \frac{1-\lambda_P}{\lambda_F}, \tag{21}$$

523 where L_c can be interpreted as the depth into the canopy to which horizontal momentum is
524 mixed before being removed by canopy drag.
525
526 3.4 Roughness length z_0 and displacement height d
527 When the density of buildings varies over short length scales, the boundary-layer flow
528 constantly evolves (see Fig. 7b), and it becomes difficult to define a roughness length
529 (Cheng and Castro 2002a). However, by dividing the study domain into overlapping stripes
530 layered in the longitudinal (streamwise) direction, we are able to estimate a gradually-
531 varying roughness length from the CFD simulation.
532 Goode and Belcher (1999) conducted a series of numerical modelling tests where the
533 terrain is composed of two different roughness lengths. They define the "blending height"
534 as the top of the roughness layer, above which the flow has "fully adjusted" to the combined
535 roughness of the terrain. They find that the wind-speed perturbation is lower than 1% when
536 the blending height is about twice the average height of the elements for that specific
537 combination of roughness lengths and other conditions. Thus, there is some evidence for
538 the pragmatic approach of determining a unique pair of z_0 and d values for various areas
539 of a city or for the entire city despite the ever-changing roughness layer. In our case, when
540 comparing each stripe, we do not find a blending height above which the wind profiles
541 agree within the 1% perturbation limit. This method of identifying the RSL depth is often
542 used in wind-tunnel studies (Kastner-Klein and Rotach 2004). Instead, we determine the

region where the fluxes are near constant with height (Feigenwinter et al. 1999; Grimmond et al. 2004; Bou-Zeid 2004), or the 'constant shear stress' region (Oke 1987), and set the lower bound of this region as the top of the roughness sublayer. We assume, as suggested by Oke (1987), that the logarithmic law can be applied in the vertical region $[z_1, z_2]$ where the shear stress is relatively constant and does not vary by more than 10%. This region differs from stripe to stripe, as shown on Fig. 10a. It is important to note that the region $[z_1, z_2]$ is defined for the IBL created by the underlying roughness elements of each stripe.

The top of the presumed logarithmic region, z_2, grows steadily as the IBL develop, from 78 m in stripe a to 106 m in stripe e, after which z_2 decreases drastically. This is due to two reasons: the fact that, as described previously, a separation between the IBL and the combined boundary layer can be noted from stripe e onwards (see Fig. 7b); and that λ_P increases while λ_F decreases for the last three stripes (see Fig. 6). On the other hand, z_1 is constantly growing above the average building height, varying between 1.7 and 2.9 (all-stripes $\approx$2.9). Moreover, $(z_2 - z_1)/h$ increases from 0.44 in stripe a to 2.4 in stripe e and then decreases to 1.0 in stripe h. In other words, the thickness of the presumed logarithmic region is constantly changing over the roughness elements, though it should be noted that, most probably, this region does not conform to a typical inertial sublayer. It has been posited (Cheng and Castro 2002b), and we confirm this, that the logarithmic law is in fact often applicable even in the RSL once the horizontal spatial heterogeneity is averaged (see Fig. 10a,c,d).

Finally, the friction velocity, $u_* = \sqrt{\tau/\rho}$, can be calculated such that each stripe has a unique u_* value. Once the logarithmic-law region of the IBL and the corresponding u_* are set for a given stripe, it is possible, using a standard nonlinear estimation algorithm, to determine d and z_0 from the logarithmic equation that is presumed to prevail in this region (Eq. 2).

568 Surface drag is dominated by the pressure drag of the buildings for all the stripes and
569 thus it is possible to calculate d directly ~~by~~ from

$$d = \frac{\int_0^{h_{max}} z\, F_1(z) dz}{\int_0^{h_{max}} F_1(z) dz}, \tag{22}$$

570 and z_0 is then fitted to the CFD data using, once more, a standard non-linear estimation
571 algorithm. Both methods yield very similar values of z_0 and d.
572 The estimated velocity component provides good fits to the actual data in every stripe.
573 As an example, the actual/estimated velocity component in this vertical region for a stripe
574 where the internal and combined boundary layers are present, stripe "f", as well as for the
575 all-stripes domain is shown in Fig. 10c, d.
576 Millward-Hopkins et al. (2011) argue that the lowest height above which a logarithmic
577 profile applies is given by

$$z_{1MH} = \begin{cases} d\frac{19.2\lambda_p[1-\exp(\lambda_p)]}{19.2\lambda_p-1+\exp(-19.2\lambda_p)} & for\ \lambda_p \geq 0.19 \\ d\frac{(1+114\lambda_p+187{\lambda_p}^3)[1-\exp(-19.2\lambda_p)]}{117\lambda_p+(187.2{\lambda_p}^3-6.1)[1-\exp(-19.2\lambda_p)]} & for\ \lambda_p < 0.19 \end{cases}, \tag{23}$$

578 while Kanda et al. (2013) claim that the height $\sigma_H + h$ is likely to be important. These
579 heights are also shown in Fig. 10a where it can be seen that both are very similar and can
580 be estimated z_1 with confidence up to stripe "e".
581

582

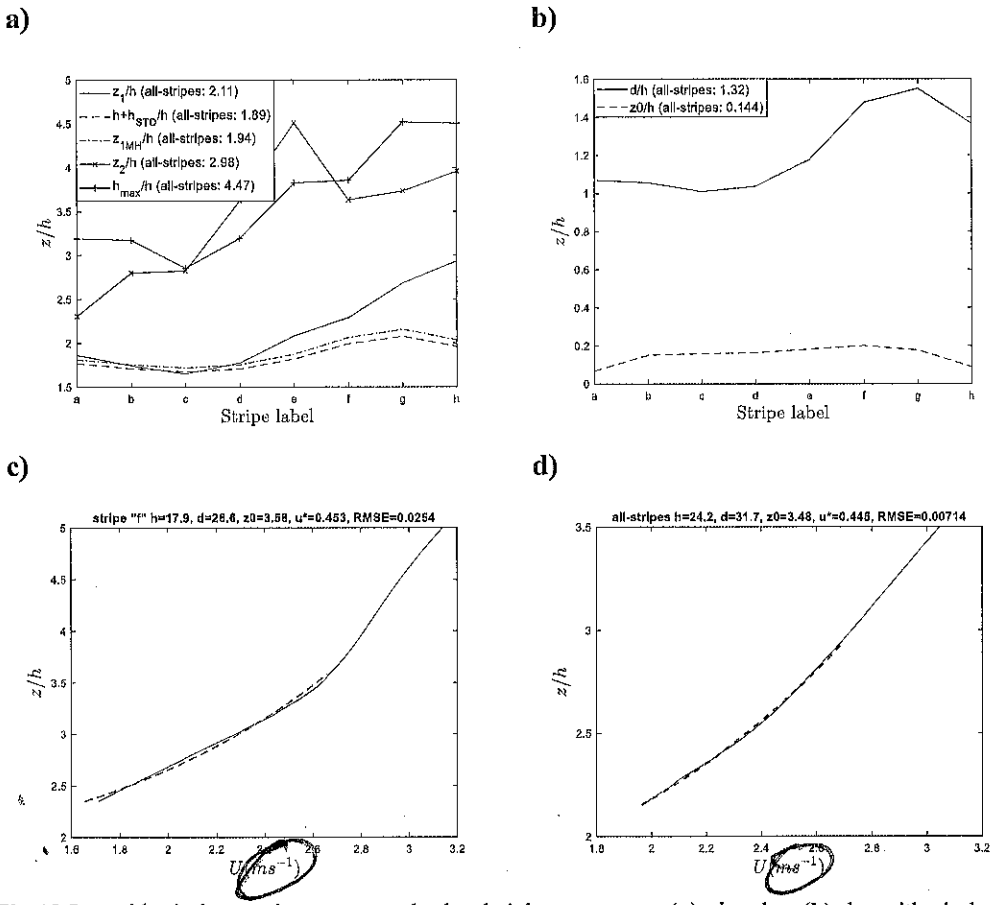

583 **Fig 10** Logarithmic-law region extent and other height parameters (**a**), d and z_0 (**b**), logarithmic-law fit in
584 $[z_1, z_2]$ for stripe f (**c**) and for the all-stripes domain (**d**)

585

586 The roughness length z_0 reaches a maximum of 5 m in stripe c and then decreases to
587 1.3 m for stripe h, a reduction which denotes the rather steep transition from dense high-
588 rise seaside stripes to less dense low-rise inland stripes. The average z_0 for the all-stripes
589 domain is 3.5 m. The variation of the displacement height d decreases in a regular manner,

590 from 48 m in stripe a to 25 m in the last stripe. In relative terms, d/h coincides with the
591 top of the canopy until stripe e; decreasing from 1.1 in stripe a to a minimum of 1.0 in stripe
592 c and then gradually growing to roughly 1.6 for stripe g. On the other hand, z_0/h grows
593 almost linearly from stripe b to f with values of 0.15 and 0.2, respectively. In relative terms,
594 d/z_0 is fairly constant for internal stripes "b" to "g" with a value of ≈ 7, which is
595 consistent with Grimmond and Oke (1999).

596 Based on an extensive review of wind-profile observations in many urban areas,
597 Grimmond and Oke (1999) concluded that z_0/h ranges from approximately 0.06 to 0.2,
598 and d/h ranges from approximately 0.35 to 0.85. Our estimated z_0/h is within the stated
599 range while our estimated d/h exceeds the maximum reported value of 0.85 in all the
600 stripes. However, experimental data show that d/h can be > 1 for surfaces of
601 heterogenous height (Cheng and Castro 2002a; Hagishima et al. 2009; Zaki et al. 2011), as
602 tall buildings dominate the aerodynamic characteristics of urban surfaces (Xie et al. 2008).

603 Following Kent et al. (2017), we compare our estimated roughness length and
604 displacement height values to those prescribed by ten prevailing formulations found across
605 the literature, four of which incorporate roughness-element height variability. They are
606 summarized in Table 3 and described in full in Appendix 1.

Reference	Abbreviation	Developed from/for	Surface type	Geometric input
Raupach (1994)	*Ra94*	Wind-tunnel and rough-surface vegetated data	Vegetated rough surface	h λ_F
Bottema and Mestayer (1998)	*Bo98*	Simplification of Bottema (1995); Bottema (1997) for use in urban areas	Regular, staggered and varying density array of blocks	h_V λ_P λ_F
Macdonald et al. (1998)	*MC98*	Fundamental principles, simple assumptions and	Staggered arrays of blocks	h λ_P

		wind-tunnel data from Hall et al. (1996)		λ_F
Grimmond and Oke (1999)	*GO99*	Wind-tunnel and field results	Cities	h
Cheng and Castro (2002b)	*CC02*	Wind-tunnel data	Staggered arrays of cubes and rectangular blocks	h
Millward-Hopkins et al. (2011)	*MH11*	Quasi-empirical modelling and development of previous models	Arrays of square-based blocks of heterogenous heights	h λ_P λ_F
Millward-Hopkins et al. (2013)	*MH13*	Simplification of the Millward-Hopkins et al. (2011) model	Arrays of square-based blocks of heterogenous heights	h σ_H $\lambda_p(z)$
Kanda et al. (2013)	*Ka13*	LES of city of Tokyo & simplified arrays	City and arrays of blocks	h h_{max} λ_P λ_F σ_H
Zhu et al. (2016)	*Zh16*	Statistical moments of variable topography through LES	Synthetic urban-like topographies	$\langle\sigma_H\rangle$ $\langle s_k\rangle$
Modified Zhu et al. (2016)	*Zhu16*	Modified model by Zhu et al. (2016)	City	σ_H s_k

607 **Table 3** Prevailing models, ordered by date, used to calculate z_0 and d from morphometric data

608

609 The *CC02* and *GO98* formulations are clearly too simple to capture the complex
610 phenomena that occur in the UCL and perform poorly across all stripes. They are not shown
611 in Fig. 11a. z_{0Bo98} is not shown in Fig. 11b as it consistently overestimates z_0 by several
612 orders of magnitude.

The displacement heights d_{Bo98} and d_{MC98} follow similar trends across all stripes and so do d_{Ka13} and d_{MH13}, where $d_{Ka13} > d_{MH13}$, which is consistent with the morphometric analysis performed by Kent et al. (2017), considering the λ_P at hand. The first two consistently underestimate d and cannot reproduce its variation with fetch, unlike the last two which, if multiplied by a coefficient <1, obtain better fits across all the stripes ($\approx$0.7 and ≈ 0.75 for *Ka13* and *MH13*, respectively). Using the least-squares method, we optimized the coefficients in the *Ka13* model for the city of Abu Dhabi: $a_0 = 1.12, b_0 = 0.81$ and $c_0 = -0.50$, giving *RMSE*=1.34m.

Overall, morphometric methods that incorporate roughness-element height variability (*MH11; MH13; Ka13; Zh16; Zhu*) agree better with the estimated d, where d_{Zhu} offers the lowest *RMSE* across all stripes and the best shape-fit. The modified version of *Zh16* (*Zhu16*) outperforms all other models and offers a very powerful morphometric method with a very simple relationship that characterizes d accurately for the city of Abu Dhabi. A value of $\alpha_d = 1.45$ achieves an almost perfect fit across all stripes, as seen in Fig. 11c. Also shown on this figure is the *MH11* model value multiplied by a correction factor of 5/8, which performs well across stripes "a" to "g".

However, none of the morphometric methods accurately predicts z_0 for all stripes. It must be noted that the *MH11* model predict values of d that are larger than h across all stripes, and therefore $z_0 < 0$ in those cases, as also occurs with the *MH13* for some stripes.

a) **b)**

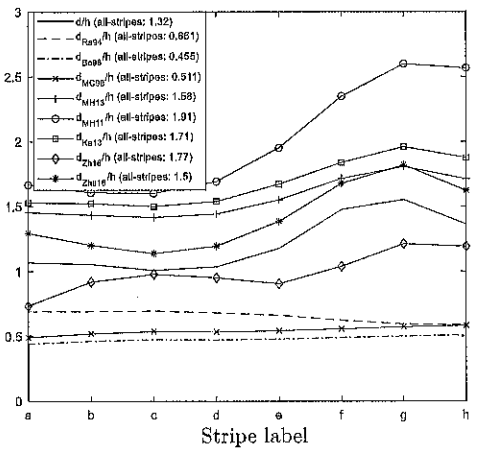

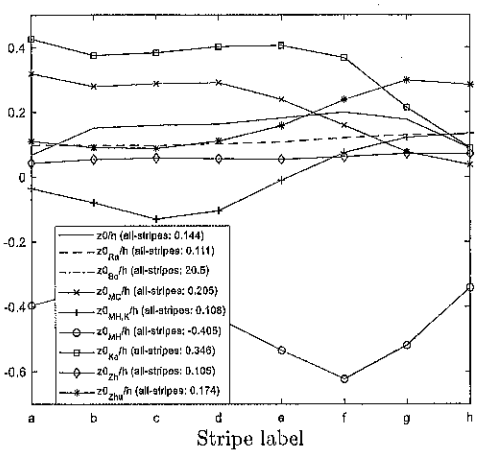

c)

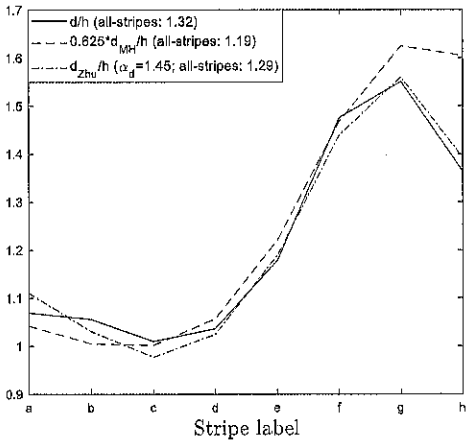

632 **Fig 11** Comparison of different morphometric methods for d **(a)** and for z_0 **(b)** and modified *MH11* and
633 *Zhu16* models **(c)**

634

635 3.5 Mixing-length model

The simplest turbulence closure models in the literature are formulated in terms of Prandtl's mixing-length (Garratt 1992). An effective, spatially-averaged mixing-length can be defined as (Coceal et al. 2006)

$$l_m(z) = \sqrt{< \overline{u_1' u_3'} >} \Big/ \frac{dU}{dz}, \tag{24}$$

so that we can calculate the value of this mixing-length using the estimated turbulent shear stress determined previously. The results are shown in Fig. 12a, where we also display values derived from the simplified model proposed by Coceal and Belcher (2004). The shape of our CFD-derived mixing-length for the all-stripes domain is similar to that reported in Fig. 21 of Coceal et al. (2006) for staggered cubic roughness elements. We observe a maximum within and above the canopy of $l(z) \approx 0.4$h and $l(z) \approx 0.5$h, respectively, in agreement with Coceal et al. (2006). Furthermore, the simplified linear approximation $\kappa(z-d)$ is applicable roughly in the vertical region $z/h = 1.75 \pm 0.25$, while for Coceal et al. (2006) the linear region was $z/h = 1.5 \pm 0.5$. Within the urban canopy, the mixing-length decreases, almost linearly, until about $0.1h$. The CFD-derived mixing-length can roughly follow the variation foreseen by Coceal et al. (2006) when varying a scaling parameter, s.

Coceal and Belcher (2004) set the mixing-length to $l(z) = \kappa(z-d)$ above the canopy, and they further assume that, within a dense canopy, $l = constant = l_c$. Since, on the other hand, the mixing-length for a sparse canopy is best modelled as $l = \kappa z$, they finally opt for a harmonic mean between the two extreme cases,

$$\frac{1}{l(z)} = \frac{1}{l_c} + \frac{1}{\kappa z} \rightarrow l(z) = \frac{1}{1/l_c + 1/\kappa z}. \tag{25}$$

Here, l_c is determined by requiring that, at the top of the canopy, the mixing-length within the canopy is $s\kappa(h-d)$, i.e. a factor s times the mixing-length in the boundary layer immediately above the canopy, or

$$\frac{1}{s\kappa(h-d)} = \frac{1}{l_c} + \frac{1}{\kappa h} \rightarrow l_c = \frac{1}{1/s\kappa(h-d) - 1/\kappa h}. \quad (26)$$

Macdonald (2000) suggests $s = 0.5$ while Coceal and Belcher (2004) prefer $s = 1$ in order to ensure continuity at $z = h$. Our results show, however, that the mixing-length lacks the expected continuity at $z = h$ and thus a value of $s = 1$ is unsupported in our case, where $s > 1$ achieves better fits.

Taking the mid-range stripe "d" as a representative example, we see that, despite the very approximate fit that the simple mixing-length model of Coceal and Belcher (2004) provides, the estimated velocity field based on this mixing-length model is surprisingly accurate (Fig 12a, b). The derivation of this wind velocity component using the simplified mixing-length model is explained below. Note that the selected value of $s = 9$ is such that the error in the estimated wind velocity component is minimized.

a)

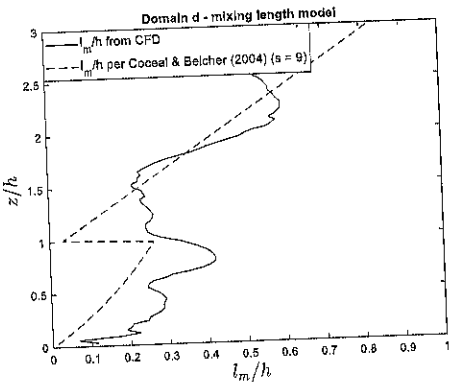

b)

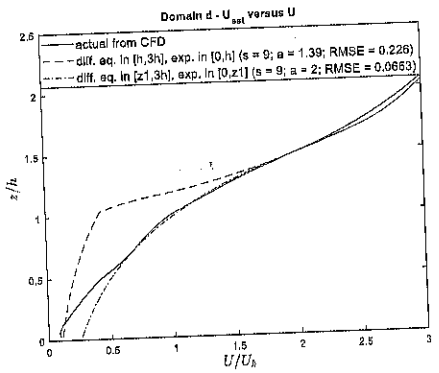

Fig 12 Mixing-length model for stripe "d" (**a**) and velocity fit for stripe "d" (**b**)

Initially, we compute the wind velocity component at the height where the drag force drops to zero (around $z/h \approx 3$ for stripe "d" – see Fig. 8). Since at that height the logarithmic profile is applicable, the derivative of the wind velocity is given by

$$\frac{dU}{dz} = \frac{u_*/\kappa}{z-d}. \tag{27}$$

Following Yang et al. (2016), and starting from known values of U and dU/dz at the top boundary, the following non-linear equation can be solved down to $z = h$

$$\frac{d}{dz}\left\{\left[l_m(z)\frac{dU}{dz}\right]^2\right\} = \sigma_F(z)U^2(z), \tag{28}$$

where,

$$\sigma_F(z) = \frac{c_d(z)\lambda_F(z)}{2h_F}. \tag{29}$$

It must be noted that Yang et al. (2016) assume that the mixing-length and drag coefficient are z-independent for simplicity, unlike in our case. For the numerical resolution, we use the differential system formulation proposed by Di Sabatino et al. (2008) combined with a stiff-problem discretization method. Due to the discontinuity of the mixing-length model (see Fig. 12a), the differential equation cannot be solved down to ground level and the numerical discretization scheme becomes unstable at canopy height. Our numerical resolution, therefore, covers only the region $z > h$.

Within the canopy ($z < h$), based on the same differential equation as above but assuming that l_m and σ_F are constant, which is not the case, the Cionco (1965) exponential formula becomes a solution of Eq. 27,

$$U(z) = U_h \exp\left[a\left(\frac{z}{h} - 1\right)\right]. \tag{30}$$

This exponential approximation is simple and describes well the laboratory experiments; however, it relies on the wind speed at the building height—the height at which the velocity profile is changing quite rapidly. For the coefficient a, Macdonald (2000) suggests $a = 9.6\lambda_F$ while Coceal and Belcher (2004) propose a more complex formula relating a to L_c and l_c:

$$a = \frac{h}{\left(2l_c^2 L_c\right)^{3/2}} \tag{31}$$

where both l_c and L_c were defined previously. Although the attenuation term a is not a universal constant, Cionco (1972) observed that, for different vegetation canopies, it usually falls in the range 2-3. In our study, based on the formulation of Coceal and Belcher (2004), a is smaller than 2. For stripe "d", its value is approximately 1.56. The resulting wind velocity for the mixing-length model in stripe "d" is displayed on Fig. 12b in comparison to the actual wind velocity component from the CFD simulation. The standard model is quite accurate although the *RMSE* of the wind velocity component in the estimation region ($z/h \in [0,3]$) exceeds 0.1. If, however, we now assume that the exponential region ends at $z = z_1$ (blending height) instead of $z = h$, and update the value of a in Eq. (30) by replacing h with z_1 (which results in $a = 2.1$), the *RMSE* is halved and the outcome is an almost perfect match in the region $z \in [0, z_1]$. Likewise, Yang et al. (2016) also assume that the exponential profile ends where the logarithmic law begins, with no transition region, in LES of several configurations of arrays of rectangular-prism elements. We posit that this extremely good fit above $0.5\ z/h$ is due to the fact that in this region the drag coefficient exhibits a fairly constant behaviour with height (Fig. 8).

While the curve does not satisfy the no-slip condition at the ground level, as mentioned by Di Sabatino et al. (2008), in reality there is a relatively thin boundary layer near the ground to satisfy this condition.

3.6 Wind speed attenuation in the urban canopy

As with ~~similar to~~ the analysis ~~done by~~ of Coceal and Belcher (2004), we compute a spatially-averaged wind velocity in the xy plane at different heights and for a large number of equally-sized overlapping stripes starting at the inlet of the CFD domain, well before the beginning of the urban canopy, and continuing well after it ends—a total fetch of 6000 m. In this way, we can plot the variation of the wind speed as a function of fetch. To maintain consistency, the variable z has been normalized everywhere using the plan area averaged height h_0 of the all-stripes domain. The wind speed is normalized by its value at the inlet of the CFD simulation domain.

The two thick vertical bars in Fig. 13 define the all-stripes domain (stripes "a" through "h"), and the ~~The~~ two thin vertical bars define, respectively, the fetch at which the first buildings appear and the fetch at which the last buildings disappear. It should be noted that the original CFD domain, a nearly square trapezoid, was structured along main street axes and included 11 distinct neighbourhoods. The stripes, on the other hand, have equal size and are overlaid in the streamwise direction, and ~~They~~ do not exactly cover the totality of the original domain. In other words, two triangular regions of the original CFD domain, upstream and downstream of the flow, are situated outside of the all-stripes domain (see Fig. 4), and ~~This~~ explains why the attenuation starts before stripe "a" begins and remains significant beyond the last stripe. Naturally these fluctuations do not warrant a detailed analysis since they correspond to an artificial situation resulting from the skewed nature of the secondary analysis domain (stripes). We focus our attention on the fetch region comprising the stripes: $x \in [1605, 3150]$. It can be seen in Fig. 13, that the attenuation at the top of the canopy reaches an extreme of 0.22, and at $z = 0.25h_0$, the attenuation reaches an extreme of 0.13. Coceal and Belcher (2004) perform a similar analysis across cubical

roughness elements where the attenuation of the wind at a height of half the element height reaches a minimum of around 0.4 within the canopy.

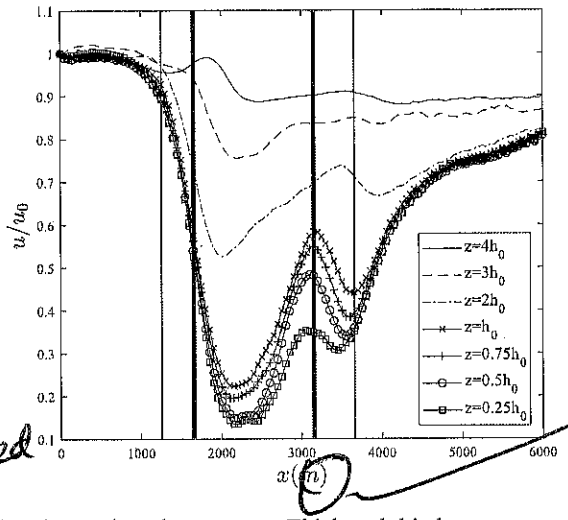

Fig 13 Velocity attenuation due to the urban canopy. Thick and thin bars represent the beginning and end of the all-stripes domain and the builtscape, respectively.

4 Conclusions

We use a steady-state RANS CFD simulation to investigate the airflow in a large portion of downtown Abu Dhabi. The study domain is subdivided into a set of overlapping stripes, overlaid along the prevailing wind direction, which allows us to analyse the evolution of the urban boundary layer as the flow penetrates into the city and the urban morphology changes. Each stripe is characterized using a novel definition of plan area and frontal area indices that introduces a variation with height, as well as other geometric parameters such as average building height. Aerodynamically, the stripes are characterized using CFD simulation results, where the sectional drag coefficient is derived from the drag force and

the proposed height-dependent morphometric indices, and the friction velocity is derived from the total (dispersive + turbulent) shear stress.

Through the determination of the friction velocity we identify a vertical region where it is almost constant and where a logarithmic law is presumed to prevail. CFD results show that the logarithmic law can indeed be applied in this region, where a best-fit approach is used to determine the displacement height and roughness length for each stripe. These values are compared to those predicted by empirical relations found across the literature. Modified versions of the models proposed by Zhu et al. (2016) and Millward-Hopkins et al. (2011) offer extremely good predictions of d. Furthermore, the model proposed by Kanda et al. (2013) for the estimation of d works well if we tune its experimentally determined coefficients in order to adapt it to the case of Abu Dhabi. On the other hand, no single model can predict z_0 with sufficient accuracy in all stripes.

We next use the sectional drag coefficient to validate the mixing-length model of Coceal and Belcher (2004) and their adaptation of the exponential relation of Cionco (1965) within the urban canopy. When compared to the CFD wind velocity component data in the all-stripes domain, the Coceal and Belcher (2004) model (which received several improvements in this study) performs exceptionally well, with an *RMSE* of 0.0653. This high accuracy was achieved by assuming that the exponential relation is applicable up to the bottom of the logarithmic-law region, corresponding to height z_1. This result can be attributed, in part, to the height dependence of the parameter σ_F, itself a function of height-dependent c_d and λ_F.

Finally, we studied the attenuation of wind speed in the urban canopy at different heights as a function of fetch, within and above the urban canopy. With the exception of small anomalies immediately before and after the urban domain—due to the fact that the overlaid stripes do not exactly coincide with the original CFD domain—the wind-speed

attenuation is more severe in a real setting than in regular cubical arrays, such as that observed by Coceal and Belcher (2004), where it reaches a minimum of around 0.4 at a height of half the element height. In our domain, at the top of the canopy the attenuation reaches an extreme of 0.22, and within the canopy, it reaches an extreme of 0.13 at a height of about 4 m.

In the most general case, for any given stripe, the lowest region of quasi-constant friction velocity defines the IBL while, above it, one often encounters a second region of constant friction velocity. The latter is referred to as the combined boundary layer since it combines the effect of preceding stripes. Given the co-existence, in most downstream stripes, of both an IBL and a combined boundary layer, it is crucial to accurately identify the region of applicability of the logarithmic law. If this determination is done carefully, we have shown that a remarkable fit between the logarithmic law and the data can be achieved resulting in reliable estimation of d and z_0.

Acknowledgments This work was funded, in part, under the Cooperative Agreement between the Masdar Institute of Science and Technology, Abu Dhabi, UAE and the Massachusetts Institute of Technology, Cambridge, MA, USA, Reference Number 02/MI/MIT/CP/11/07633/GEN/G/00. The wind speed/direction data used for model validation was measured by two weather monitoring stations operated by the Environmental Agency of Abu Dhabi (EAD).

5 Appendix 1

We compare our estimated roughness length and displacement height values to those prescribed by ten prevailing formulations found across the literature, four of which incorporate roughness-element height variability.

799 Originally derived for vegetated surfaces, the *Ra94* method provides reasonably
800 accurate results in urban environments (Bottema and Mestayer 1998; Grimmond and Oke
801 1999),

$$d_{Ra94} = \left[1 + \left(\frac{\exp[-(C_{dl}2\lambda_F)^{0.5}]-1}{(C_{dl}2\lambda_F)^{0.5}}\right)\right]h, \tag{32}$$

$$z_{0\mathrm{Ra94}} = \left[\left(1 - \frac{d_{Ra}}{h}\right)\exp\left(-k\frac{U(h)}{u_*} + \psi_h\right)\right]h, \tag{33}$$

802 where

$$\frac{u_*}{U(h)} = \min\left[(C_S + C_{Dv}\lambda_F)^{0.5}, \left(\frac{u_*}{U(h)}\right)_{max}\right]. \tag{34}$$

803 Here, C_S and C_{Dv} are the drag coefficients for the substrate surface at height h in the
804 absence of roughness elements, and of an isolated roughness element mounted on the
805 surface, respectively; C_{dl} is a free parameter, ψ_h is the RSL influence function and $U(h)$
806 and u_* are the wind speed at the average roof height and the friction velocity, respectively.
807 The values specified by Raupach (1994) are: $C_S = 0.003, C_{Dv} = 0.3, \psi_h = 0.193, C_{dl} =$
808 7.5 and $(u_*/U(h))_{max} = 0.3$. Although these constants vary depending on roughness
809 elements (Bottema and Mestayer 1998), a sensitivity analysis is beyond the scope of the
810 present study.

811 The *Bo98* method is a simplification of Bottema (1995); Bottema (1997) for use in
812 urban areas. The method assumes that all of the drag experienced by the flow is due to
813 substrate roughness and includes a mutual sheltering parameter,

$$d_{Bo98} = {\lambda_P}^{0.6}h, \tag{35}$$

$$z_{0\mathrm{Bo98}} = (h_V - d_{Bo98})\exp\left(-\frac{k}{(0.5\,C_{dh}\,\lambda_F)^{0.5}}\right)h, \tag{36}$$

814 where C_{dh} is the drag coefficient of buildings. Instead of the prescribed value of 0.8 for an
815 isolated obstacle, we use the calculated value for each stripe.

816 The empirical formulations of Macdonald et al. (1998) include a drag correction
817 coefficient, β, and a fitting constant, α, that controls the increase of d/h with λ_p

$$d_{MC98} = \left[1 + \alpha^{-\lambda_p}(\lambda_p - 1)\right]h, \tag{37}$$

$$z_{0MC98} = \left[\left(1 - \frac{d_{MC98}}{h}\right)\exp\left\{-\left[0.5\,\beta\,\frac{C_{dh}}{\kappa^2}\left(1 - \frac{d_{MC98}}{h}\right)\right]^{-0.5}\right\}\right]h, \tag{38}$$

818 where Macdonald et al. (1998) suggest $C_{dh} = 1.2$ and, based on wind-tunnel data from Hall
819 et al. (1996), $\alpha = 4.43$, and $\beta = 1$ for staggered arrays, and $\alpha = 3.59$, and $\beta = 0.55$ for
820 square arrays. The former coefficients are used, along with the calculated value of C_{dh} for
821 each stripe.

822 The simplest method, often called the "rule-of-thumb" relates the average building
823 height to z_0 and d through a coefficient. Both *GO98* and *CC02* methods suggest values of
824 $d_{GO98} = 0.7h$, $z_{0GO98} = 0.1h$ and $d_{CC02} = 0.83h$, $z_{0CC02} = 0.053h$. It is unclear how
825 accurate all the above-mentioned ~~formulas~~ relations are when applied to actual towns and cities, as
826 there have been no studies to test their validity for non-cubic arrays (Padhra 2010).

827 Four morphometric methods that incorporate variable roughness-element heights are
828 tested: *MH11, MH13, Ka13* and *Zh16*. The first method divides the urban canopy into
829 layers and calculates a cumulative-height normalized d and drag balance, based on
830 uniform arrays and an attenuation coefficient proposed by Macdonald (2000). Kent et al.
831 (2017) argue that this process is ~~complicated~~ overly ex and thus a relation based on the standard
832 deviation of roughness-element heights has been developed (Millward-Hopkins et al.
833 2013)

$$d_{MH13} = \left[\frac{f_{d,MH13}}{h} + \left(\left(0.2375ln(\lambda_p) + 1.1738\right)\frac{\sigma_h}{h}\right)\right]h, \tag{39}$$

$$z_{0MH13} = \left[\frac{f_{0,MH13}}{h} + \left(\exp(0.8867\lambda_f) - 1\right)\left(\frac{\sigma_h}{h}\right)^{\exp(2.3271\lambda_f)}\right]h, \tag{40}$$

where,

$$f_{d,MH13} = \begin{cases} \frac{19.2\lambda_p - 1 + \exp(-19.2\lambda_p)}{19.2\lambda_p[1-\exp(\lambda_p)]} & for\ \lambda_p \geq 0.19 \\ \frac{117\lambda_p + (187.2\lambda_p{}^3 - 6.1)[1-\exp(-19.2\lambda_p)]}{(1+114\lambda_p+187\lambda_p{}^3)[1-\exp(-19.2\lambda_p)]} & for\ \lambda_p < 0.19 \end{cases} \quad (41)$$

$$f_{0,MH13} = \left(1 - \frac{d_{MH13}}{h}\right) \exp\left[-\left(0.5 C_{dh} \kappa^{-2} \lambda_p\right)^{-0.5}\right] h, \quad (42)$$

However, with height-dependent morphological indexes, we are able to re-write the relations originally proposed by Millward-Hopkins et al. (2011) such that

$$d_{MH11} = \int_0^{h_{max}} f_{d,MH11}\left(\lambda_p(z)\right) dz, \quad (43)$$

$$z_{0MH11} = \left(1 - \frac{d_{MH11}}{h}\right) \exp\left[-\left(0.5 C_{dh} \kappa^{-2} \lambda_p(0)\right)^{-0.5}\right] h, \quad (44)$$

where,

$$f_{d,MH11}\left(\lambda_p(z)\right) = \begin{cases} \frac{19.2\lambda_p(z) - 1 + \exp\left(-19.2\lambda_p(z)\right)}{19.2\lambda_p(z)\left[1-\exp\left(\lambda_p(z)\right)\right]} h & for\ \lambda_p(z) \geq 0.19 \\ \frac{117\lambda_p(z) + \left(187.2\lambda_p(z)^3 - 6.1\right)\left[1-\exp\left(-19.2\lambda_p(z)\right)\right]}{\left(1+114\lambda_p(z)+187\lambda_p(z)^3\right)\left[1-\exp\left(-19.2\lambda_p(z)\right)\right]} h & for\ \lambda_p(z) < 0.19 \end{cases} \quad (45)$$

Once more, the calculated value of C_{dh} for each stripe is used.

The *Ka13* model is derived based on horizontally-averaged statistics of LES of the city of Tokyo and simple arrays from the literature. Aerodynamic parameters are determined through a least-square regression and an empirical model based on five geometric parameters. Kanda et al. (2013) argue that h_{max} is a more suitable scaling parameter than h as it is found to coincide with the upper limit of d, such that

$$d_{Ka13} = \left[c_0 X^2 + \left(a_0 \lambda_p^{b_0} - c_0\right) X\right] h_{max}, \quad (46)$$

where $a_0 = 1.29$, $b_0 = 0.36$ and $c_0 = -0.17$. X is the representative building height above the average building height ($\sigma_h + h$), relative to the maximum building height,

$$X = \frac{\sigma_h + h}{h_{max}} \quad for\ 0 \le X \le 1. \tag{47}$$

The roughness length in the *Ka13* method is a modification to that of *MC98*,

$$z_{0Ka13} = (b_1 Y^2 + c_1 Y + a_1)\, z_{0MC98}, \tag{48}$$

where $Y = \frac{\lambda_p \sigma_h}{h}$ for $0 \le Y$, and $a_1 = 0.71$, $b_1 = 20.21$ and $c_1 = -0.77$ are empirically derived coefficients. The impact of λ_p and σ_h on z_0 is accounted for by Y, which tends to zero for homogenous arrays.

Finally, the *Zh16* model has been derived through LES of urban-like topographies wherein statistical moments of the topography have been systematically varied (Zhu et al. 2016). They find that there is a strong relationship between d and the standard deviation of building heights, considering ground area, such that

$$d_{Zh16} = \alpha_d \langle \sigma_h \rangle, \tag{49}$$

where $\alpha_d = 1.69$. Similarly, they find strong dependencies between z_0, $\langle \sigma_h \rangle$ and $\langle s_k \rangle$, and propose a hybrid roughness correlation between the Flack and Schultz (2010) and Ito et al. (2011) models

$$z_{0Zh16} = \begin{cases} \alpha \langle \sigma_h \rangle (1 + \beta \langle s_k \rangle) & for\ \langle \sigma_h \rangle / \langle h \rangle < 1.15 \\ \alpha \langle \sigma_h \rangle (1 + \langle s_k \rangle)^{\beta} & for\ \langle \sigma_h \rangle / \langle h \rangle \ge 1.15 \end{cases}, \tag{50}$$

where the model parameters, $\alpha \approx 0.1$ and $\beta = 0.9$, have been tuned for atmospheric flows over urban-like topographies. Traditional geometric parameters that do not consider ground surface (h, σ_h and s_k) were also used to test the above model giving d_{Zhu16} and z_{0Zhu16}.

862 **6 References**

863 Assimakopoulos VD, ApSimon HM, Moussiopoulos N (2003) A numerical study of atmospheric pollutant
864 dispersion in different two-dimensional street canyon configurations. Atmos Environ 37(29):4037-4049
865 Baik JJ, Kim JJ (1999) A numerical study of flow and pollutant dispersion characteristics in urban street
866 canyons. J Appl Meteorol 38(11):1576-1589
867 Barlow JF (2014) Progress in observing and modelling the urban boundary layer. Urban Clim 10:216-240
868 Barlow JF, Dunbar TM, Nemitz EG, Wood CR, Gallagher MW, Davies F, O'Connor E, Harrison RM (2011)
869 Boundary layer dynamics over London, UK, as observed using Doppler lidar during REPARTEE-II.
870 Atmos Chem Phys 11:2111-2125
871 Barlow JF, Harman IN, Belcher SE (2004) Scalar fluxes from urban street canyons. Part I: Laboratory
872 simulation. Boundary-Layer Meteorol 113:369-385 doi:10.1007/s10546-004-6204-8
873 Bartzis JG, Vlachogiannis D, Sfetsos A (2004) Thematic area 5: Best practice advice for environmental flows.
874 The QNET-CFD Network Newsletter 2(4):34:39
875 Blocken B (2015) Computational Fluid Dynamics for urban physics: Importance, scales, possibilities,
876 limitations and ten tips and tricks towards accurate and reliable simulations. Build Environ 91:219-245
877 doi:10.1016/j.buildenv.2015.02.015
878 Bottema M (1995) Aerodynamic roughness parameters for homogeneous building groups - Part 2: Results.
879 Technical Report SUB-MESO #23, Ecole Centrale de Nantes, France, 80pp.
880 Bottema M (1997) Urban roughness modelling in relation to pollutant dispersion. Atmos Environ 31:3059-
881 3075 doi:10.1016/S1352-2310(97)00117-9
882 Bottema M, Mestayer PG (1998) Urban roughness mapping - validation techniques and some first results. J
883 Wind Eng Industr Aerodyn 74-76:163-173. doi:10.1016/S0167-6105(98)00014-2
884 Bou-Zeid E (2004) Large-eddy simulation of neutral atmospheric boundary layer flow over heterogeneous
885 surfaces: Blending height and effective surface roughness. Water Resour Res 40:1-18
886 doi:10.1029/2003WR002475
887 Brown MJ, Lawson RE, DeCroix DS, Lee RL (2001) Comparison of centerline velocity measurements
888 obtained around 2D and 3D building arrays in a wind-tunnel. In: Proceedings of the International Society
889 for Environmental Hydraulics, 5-8 December, 2001, Tempe, Arizaona, USA
890 Chan AT, Au WTW, So ESP (2003) Strategic guidelines for street canyon geometry to achieve sustainable
891 street air quality - Part II: Multiple canopies and canyons. Atmos Environ 37(20):2761-2772
892 doi:10.1016/S1352-2310(03)00252-8
893 Cheng H, Castro IP (2002a) Near-wall flow development after a step change in surface roughness. Boundary-
894 Layer Meteorol 105:411-432 doi:10.1023/A:1020355306788
895 Cheng H, Castro IP (2002b) Near-wall flow over urban-like roughness. Boundary-Layer Meteorol 104
896 (2):229-259 doi:10.1023/a:1016060103448
897 Cheng Y, Lien FS, Yee E, Sinclair R (2003) A comparison of large eddy simulations with a standard k-ε
898 Reynolds-averaged Navier-Stokes model for the prediction of a fully developed turbulent flow over a
899 matrix of cubes. J Wind Eng Industr Aerodyn 91 (11):1301-1328 doi:10.1016/j.jweia.2003.08.001
900 Christen A (2005) Atmospheric turbulence and surface energy exchange in urban environments—Results
901 from the Basel Urban Boundary Layer Experiment (BUBBLE). Thesis, University of Basel, Basel,
902 Switzerland
903 Cionco RM (1965) A mathematical model for air-flow in a vegetative canopy. J Appl Meteorol 4:517-522
904 doi:10.1175/1520-0450

905 Cionco RM (1972) A wind-profile index for canopy flow. Boundary-Layer Meteorol 3:255-263
906 doi:10.1007/BF02033923
907 Coceal O, Belcher SE (2004) A canopy model of mean winds through urban areas. Q J R Meteorol Soc
908 130:1349-1372
909 Coceal O, Dobre A, Thomas TG (2007) Unsteady dynamics and organized structures from DNS over an
910 idealized building canopy. Int J Climatol 27:1943-1953 doi:10.1002/joc.1549
911 Coceal O, Thomas TG, Castro IP, Belcher SE (2006) Mean flow and turbulence statistics over groups of
912 urban-like cubical obstacles. Boundary-Layer Meteorol 121(3):491-519 doi:10.1007/s10546-006-9076-2
913 Counehan J (1971) Wind-tunnel determination of the roughness length as a function of the fetch and the
914 roughness density of three-dimensional roughness elements. Atmos Environ 5:637-642
915 doi:10.1016/0004-6981(71)90120-X
916 Cowan IR, Castro IP, Robins AG (1997) Numerical considerations for simulations of flow and dispersion
917 around buildings. J Wind Eng Industr Aerodyn 67:535-545 doi:10.1016/S0167-6105(97)00098-6
918 Cushman-Roisin B (2014) Environmental Fluid Mechanics. John Wiley & Sons, New York
919 Di Sabatino S, Solazzo E, Paradisi P, Britter R (2008) A simple model for spatially-averaged wind profiles
920 within and above an urban canopy. Boundary-Layer Meteorol 127:131-151 doi:10.1007/s10546-007-
921 9250-1
922 Dobre A, Arnold S, Smalley R, Boddy J, Barlow J, Tomlin A, Belcher S (2005) Flow field measurements in
923 the proximity of an urban intersection in London, UK. Atmos Environ 39:4647-4657
924 doi:10.1016/j.atmosenv.2005.04.015
925 Drew DR, Barlow JF, Lane SE (2013) Observations of wind speed profiles over Greater London, UK, using
926 a Doppler lidar. J Wind Eng Industr Aerodyn 121:98-105 doi:10.1016/j.jweia.2013.07.019
927 Emeis S (2011) Surface-Based Remote Sensing of the Atmospheric Boundary Layer. Springer, Netherlands
928 doi:10.1007/978-90-481-9340-0
929 Emeis S, Baumann-Stanzer K, Piringer M, Kallistratova M, Kouznetsov R, Yuhkov V (2007) Wind and
930 turbulence in the urban boundary layer - Analysis from acoustic remote sensing data and fit to analytical
931 relations. Meteorol Z 16:393-406 doi:10.1127/0941-2948/2007/0217
932 Emeis S, Münkel C, Vogt S, Müller WJ, Schäfer K (2004) Atmospheric boundary-layer structure from
933 simultaneous SODAR, RASS, and ceilometer measurements. Atmos Environ 38:273-286
934 doi:10.1016/j.atmosenv.2003.09.054
935 Erell E, Pearlmutter D, Williamson TJTJ (2012) Urban microclimate: designing the spaces between buildings.
936 Routledge, London
937 Fang C, Sill BL (1992) Aerodynamic roughness length: Correlation with roughness elements. J Wind Eng
938 Industr Aerodyn 41:449-460 doi:10.1016/0167-6105(92)90444-F
939 Feigenwinter C, Vogt R, Parlow E (1999) Vertical structure of turbulence above an urban canopy. Theor
940 Appl Climatol 62:51-63
941 Fernando HJS (2010) Fluid dynamics of urban atmospheres in complex terrain. Annu Rev Fluid Mech
942 42:365-389 doi:10.1146/annurev-fluid-121108-145459
943 Finnigan J (2000) Turbulence in plant canopies. Annu Rev Fluid Mech 32:519-571
944 doi:10.1146/annurev.fluid.32.1.519
945 Flack KA, Schultz MP (2010) Review of hydraulic roughness scales in the fully rough regime. J Fluids Eng
946 132(4):0412031-04120310 doi:10.1115/1.4001492
947 Franke J (2006) Recommendations of the COST action C14 on the use of CFD in predicting pedestrian wind
948 environment. In: Proceedings of the Fourth International Symposium on Computational Wind
949 Engineering, 16 July, 2006, Yokohoma, Japan, pp 529-532

950 Franke J, Hellsten A, Schlunzen KH, Carissimo B (2011) The COST 732 Best Practice Guideline for CFD
951 simulation of flows in the urban environment: a summary. Int J Environ Pollut 44:419-427
952 doi:10.1504/IJEP.2011.038443
953 Franke J, Hirsch C, Jensen AG, Krüs HW, Schatzmann M, Westbury PS, Miles SD, Wisse JA, Wright NG
954 (2004) Recommendations on the use of CFD in wind engineering. International conference on urban wind
955 engineering and building aerodynamics. COST action C14 Report, *Impact of wind and storm on city life*
956 *built environment.* Von Karman Institute, Sint-Genesius, Belgium
957 Garratt JR (1992) The atmospheric boundary layer. Cambridge University Press, Cambridge, 316 pp
958 Gerdes F, Olivari D (1999) Analysis of pollutant dispersion in an urban street canyon. J Wind Eng Industr
959 Aerodyn 82(1):105-124 doi:10.1016/S0167-6105(98)00216-5
960 Giometto M, Christen A, Meneveau C, Fang J, Krafczyk M, Parlange M (2016) Spatial characteristics of
961 roughness sublayer mean flow and turbulence over a realistic urban surface. Boundary-Layer Meteorol
962 160(3):425-452 doi:101007/s10546-016-0157-6
963 Giometto MG, Christen A, Egli PE, Schmid MF, Tooke RT, Coops NC, Parlange MB (2017) Effects of trees
964 on mean wind, turbulence and momentum exchange within and above a real urban environment. Adv
965 Water Resour 106:154-168 doi:10.1016/j.advwatres.2017.06.018
966 Goode K, Belcher SE (1999) On the parameterisation of the effective roughness length for momentum
967 transfer over heterogeneous terrain. Boundary-Layer Meteorol 93(1):133-154
968 doi:10.1023/A:1002035509882
969 Grimmond CSB, King TS, Roth M, Oke TR (1998) Aerodynamic Roughness of urban areas derived from
970 wind observations. Boundary-Layer Meteorol 89:1-24 doi:10.1023/A:1001525622213
971 Grimmond CSB, Oke TR (1999) Aerodynamic properties of urban areas derived from analysis of surface
972 form. J Appl Meteorol 38(9):1262-1292
973 Grimmond CSB, Salmond JA, Oke TR, Offerle B, Lemonsu A (2004) Flux and turbulence measurements at
974 a densely built-up site in Marseille: Heat, mass (water and carbon dioxide), and momentum. J Geophys
975 Res109:D24101 doi:10.1029/2004JD004936
976 Hagishima A, Tanimoto J, Nagayama K, Meno S (2009) Aerodynamic parameters of regular arrays of
977 rectangular blocks with various geometries. Boundary-Layer Meteorol 132(2):315-337
978 doi:10.1007/s10546-009-9403-5
979 Hall DJ, Macdonald R, Walker S, Spanton AM (1996) Measurements of dispersion within simulated urban
980 arrays - A small scale wind-tunnel study. Building Research Establishment Client Report 178/96
981 Hanna SR, Tehranian S, Carissimo B, Macdonald RW, Lohner R (2002) Comparisons of model simulations
982 with observations of mean flow and turbulence within simple obstacle arrays. Atmos Environ
983 36(32):5067-5079 doi:10.1016/S1352-2310(02)00566-6
984 Ito T, Matsumoto A, Ito T, Motozawa M, Iwamoto K, Kawashima H, Ando H, Senda T, Kawaguchi Y (2011)
985 Experimental investigation on effects of surface roughness geometry affecting to flow resistance. In:
986 Proceedings of the ASME-JSME-KSME 2011 Joint Fluids Engineering Conference, pp 3945-3954.
987 doi:10.1115/AJK2011-25014
988 Kanda M, Inagaki A, Miyamoto T, Gryschka M, Raasch S (2013) A new aerodynamic parametrization for
989 real urban surfaces. Boundary-Layer Meteorol 148:357-377 doi:10.1007/s10546-013-9818-x
990 Kanda M, Moriwaki R, Kasamatsu F (2004) Large-eddy simulation of turbulent organized structures within
991 and above explicity resolved cube arrays. Boundary-Layer Meteorol 112(2):343-368
992 doi:10.1023/B:BOUN.0000027909.40439.7c
993 Kastner-Klein P, Plate EJ (1999) Wind-tunnel study of concentration fields in street canyons. Atmos Environ
994 33:3973-3979 doi:10.1016/S1352-2310(99)00139-9

995 Kastner-Klein P, Rotach MW (2004) Mean flow and turbulence characteristics in an urban roughness
996 sublayer. Boundary-Layer Meteorol 111:55-84 doi:10.1023/B:BOUN.0000010994.32240.b1
997 Kent CW, Grimmond S, Barlow J, Gatey D, Kotthaus S, Lindberg F, Halios CH (2017) Evaluation of urban
998 local-scale aerodynamic parameters: implications for the vertical profile of wind speed and for source
999 areas. Boundary-Layer Meteorol 164:1-31 doi:10.1007/s10546-017-0248-z
1000 Lane SE, Barlow JF, Wood CR (2013) An assessment of a three-beam Doppler lidar wind profiling method
1001 for use in urban areas. J Wind Eng Industr Aerodyn 119:53-59 doi:10.1016/j.jweia.2013.05.010
1002 Lettau H (1969) Note on aerodynamic roughness-parameter estimation on the basis of roughness-element
1003 description. J Appl Meteorol 8:828-832
1004 Letzel MO, Krane M, Raasch S (2008) High resolution urban large-eddy simulation studies from street
1005 canyon to neighbourhood scale. Atmos Environ 42:8770-8784 doi:10.1016/j.atmosenv.2008.08.001
1006 Li QS, Zhi L, Hu F (2010) Boundary layer wind structure from observations on a 325 m tower. J Wind Eng
1007 Industr Aerodyn 98:818-832 doi:10.1016/j.jweia.2010.08.001
1008 Lien FS, Yee E (2004) Numerical modelling of the turbulent flow developing within and over a 3-D building
1009 array, part I: A high-resolution Reynolds-averaged Navier-Stokes approach. Boundary-Layer Meteorol
1010 112(3):427-466 doi:10.1023/B:BOUN.0000030654.15263.35
1011 Lien FS, Yee E (2005) Numerical modelling of the turbulent flow developing within and over a 3-D building
1012 array, part III: A distributed drag force approach, its implementation and application. Boundary-Layer
1013 Meteorol 114(2):287-313 doi:10.1007/s10546-004-1987-1
1014 Macdonald RW (2000) Modelling the mean velocity profile in the urban canopy layer. Boundary-Layer
1015 Meteorol 97:25-45 doi:10.1023/A:1002785830512
1016 Macdonald RW, Griffiths RF, Hall DJ (1998) An improved method for the estimation of surface roughness
1017 of obstacle arrays. Atmos Environ 32:1857-1864 doi:10.1016/S1352-2310(97)00403-2
1018 Martilli A, Santiago JL (2007) CFD simulation of airflow over a regular array of cubes. Part II: Analysis of
1019 spatial average properties. Boundary-Layer Meteorol 122:635-654 doi:10.1007/s10546-006-9124-y
1020 Masson V (2000) A physically based scheme for the urban energy budget in atmospheric models. Boundary-
1021 Layer Meteorol 94: 357-397 doi: 10.1023/A:1002463829265
1022 Meinders ER, Hanjalić K (1999) Vortex structure and heat transfer in turbulent flow over a wall-mounted
1023 matrix of cubes. Int J Heat Fluid Flow 20(3):255-267 doi:10.1016/S0142-727X(99)00016-8
1024 Meroney RN, Pavageau M, Rafailidis S, Schatzmann M (1996) Study of line source characteristics for 2-D
1025 physical modelling of pollutant dispersion in street canyons. J Wind Eng Industr Aerodyn 62(1):37-56
1026 doi:10.1016/S0167-6105(96)00057-8
1027 Michioka T, Takimoto H, Sato A (2014) Large-eddy simulation of pollutant removal from a three-
1028 dimensional street canyon. Boundary-Layer Meteorol 150:259-275 doi:10.1007/s10546-013-9870-6
1029 Millward-Hopkins JT, Tomlin AS, Ma L, Ingham D, Pourkashanian M (2011) Estimating aerodynamic
1030 parameters of urban-like surfaces with heterogeneous building heights. Boundary-Layer Meteorol 141
1031 (3):443-465 doi:10.1007/s10546-011-9640-2
1032 Millward-Hopkins JT, Tomlin AS, Ma L, Ingham DB, Pourkashanian M (2013) Aerodynamic parameters of
1033 a UK city derived from morphological data. Boundary-Layer Meteorol 146:447-468 doi:10.1007/s10546-
1034 012-9761-2
1035 Oke TR (1987) Boundary layer climates. Methven, London ~~435 pp~~
1036 Padhra A (2010) Estimating the sensitivity of urban surface drag to building morphology. Dissertation,
1037 University of Reading, Reading, UK

Pascheke F, Leitl B, Schatzmann M (2005) Dispersion of traffic pollutants in street canyons - Systematic wind-tunnel study to evaluate a field tracer experiment. Proceedings of the 5th International Conference on Urban Air Quality, 29-31 March 2005, Valencia, Spain, [illegible] pp

Pelliccioni A, Monti P, Leuzzi G (2016) Wind-speed profile and roughness sublayer depth modelling in urban boundary layers. Boundary-Layer Meteorol 160:225-248 doi:10.1007/s10546-016-0141-1

Poggi D, Katul GG, Albertson JD (2004) A note on the contribution of dispersive fluxes to momentum transfer within canopies. Boundary-Layer Meteorol 111:615-621 doi:10.1023/B:BOUN.0000016563.76874.47

Ramponi R, Blocken B, de Coo LB, Janssen WD (2015) CFD simulation of outdoor ventilation of generic urban configurations with different urban densities and equal and unequal street widths. Build Environ 92:152-166 doi:10.1016/j.buildenv.2015.04.018

Raupach MR (1992) Drag and drag partition on rough surfaces. Boundary-Layer Meteorol 60:375-395 doi:10.1007/BF00155203

Raupach MR (1994) Simplified expressions for vegetation roughness length and zero-plane displacement as functions of canopy height and area index. Boundary-Layer Meteorol 71:211-216 doi:10.1007/BF00709229

Raupach MR, Shaw RH (1982) Averaging procedures for flow within vegetation canopies. Boundary-Layer Meteorol 22:79-90 doi:10.1007/BF00128057

Raupach MR, Thom AS, Edwards I (1980) A wind-tunnel study of turbulent flow close to regularly arrayed rough surfaces. Boundary-Layer Meteorol 18:373-397 doi:10.1007/BF00119495

Richards PJ, Hoxey RP (1993) Appropriate boundary conditions for computational wind engineering models using the k-ε turbulence model. J Wind Eng Industr Aerodyn 46-47(C):145-153 doi:10.1016/0167-6105(93)90124-7

Rotach M (1995) Profiles of turbulence statistics in and above an urban street canyon. Atmos Environ 29:1473-1486 doi:10.1016/1352-2310(95)00084-C

Sadique J, Yang XIA, Meneveau C, Mittal R (2017) Aerodynamic properties of rough surfaces with high aspect-ratio roughness elements: effect of aspect ratio and arrangements. Boundary-Layer Meteorol 163 (2):203-224 doi:10.1007/s10546-016-0222-1

Santamouris MM, Asimakopoulos DNDN (2001) Energy and climate in the urban built environment. Routledge, London 402 pp

Santiago JL, Martilli A, Martín F (2007) CFD simulation of airflow over a regular array of cubes. Part I: Three-dimensional simulation of the flow and validation with wind-tunnel measurements. Boundary-Layer Meteorol 122:609-634 doi:10.1007/s10546-006-9123-z

Sini JF, Anquetin S, Mestayer PG (1996) Pollutant dispersion and thermal effects in urban street canyons. Atmos Environ 30(15):2659-2677 doi:10.1016/1352-2310(95)00321-5

Stoesser T, Mathey F, Frohlich J, Rodi W (2003) LES of flow over multiple cubes. ERCOFTAC Bull 56:15-19

Toda M, Sugita M (2003) Single level turbulence measurements to determine roughness parameters of complex terrain. J Geophys Res Atmos 108:D12 doi:10.1029/2002JD002573

Tominaga Y, Mochida A, Yoshie R, Kataoka H, Nozu T, Yoshikawa M, Shirasawa T (2008) AIJ guidelines for practical applications of CFD to pedestrian wind environment around buildings. J Wind Eng Industr Aerodyn 96:1749-1761 doi:10.1016/j.jweia.2008.02.058

Vachon G, Louka P, Rosant JM, Mestayer P, Sini JF (2001) Measurements of traffic-induced turbulence within a street canyon during the Nantes '99 experiment. Third International Conference on Urban Air Quality, 19-23 March, 2001, Loutraki, Greece, 19-23 March 2001

1083 Wieringa J (1992) Updating the Davenport roughness classification. J Wind Eng Industr Aerodyn 41:357-
1084 368 doi:10.1016/0167-6105(92)90434-C
1085 Wood CR, Lacser A, Barlow JF, Padhra A, Belcher SE, Nemitz E, Helfter C, Famulari D, Grimmond CSB
1086 (2010) Turbulent flow at 190 m height above London During 2006–2008: A climatology and the
1087 applicability of similarity theory. Boundary-Layer Meteorol 137:77-96 doi:10.1007/s10546-010-9516-x
1088 Xie ZT (2011) Modelling street-scale flow and dispersion in realistic winds—towards coupling with
1089 mesoscale meteorological models. Boundary-Layer Meteorol 141:53-75 doi:10.1007/s10546-011-9629-
1090 x
1091 Xie ZT, Castro IP (2006) LES and RANS for turbulent flow over arrays of wall-mounted obstacles. Flow
1092 Turbul Combust 76:291-312 doi:10.1007/s10494-006-9018-6
1093 Xie ZT, Coceal O, Castro IP (2008) Large-eddy simulation of flows over random urban-like obstacles.
1094 Boundary-Layer Meteorol 129:1-23 doi:10.1007/s10546-008-9290-1
1095 Yang XIA, Sadique J, Mittal R, Meneveau C (2016) Exponential roughness layer and analytical model for
1096 turbulent boundary layer flow over rectangular-prism roughness elements. J Fluid Mech 789:127-165
1097 doi:10.1017/jfm.2015.687
1098 Zaki SA, Hagishima A, Tanimoto J, Ikegaya N (2011) Aerodynamic parameters of urban building arrays with
1099 random geometries. Boundary-Layer Meteorol 138:99-120 doi:10.1007/s10546-010-9551-7
1100 Zhu X, Iungo GV, Leonardi S, Anderson W (2016) Parametric study of urban-like topographic statistical
1101 moments relevant to a priori modelling of bulk aerodynamic parameters. Boundary-Layer
1102 Meteorol162:231-253 doi:10.1007/s10546-016-0198-x

1103